PHYSICAL REVIEW B **105**, 115119 (2022)

Rotoinversion-symmetric bulk-hinge correspondence and its applications to higher-order Weyl semimetals

Yutaro Tanaka,[1] Ryo Takahashi,[1] Ryo Okugawa,[2] and Shuichi Murakami[1,3]
[1]Department of Physics, Tokyo Institute of Technology, 2-12-1 Ookayama, Meguro-ku, Tokyo 152-8551, Japan
[2]Graduate School of Information Sciences, Tohoku University, Sendai 980-8579, Japan
[3]Tokodai Institute for Element Strategy, Tokyo Institute of Technology, 2-12-1 Ookayama, Meguro-ku, Tokyo 152-8551, Japan

(Received 29 November 2021; accepted 1 March 2022; published 14 March 2022)

We give a bulk-hinge correspondence for higher-order topological phases protected by rotoinversion $C_4\mathcal{I}$ symmetry in magnetic systems. Our approach allows us to show the emergence of the chiral hinge modes only from the information of the $C_4\mathcal{I}$ eigenvalues at the high-symmetry points in the Brillouin zone. In addition, based on the bulk-hinge correspondence, we propose a class of higher-order Weyl semimetals (HOWSMs) being Weyl semimetals with hinge modes and Fermi-arc surface states. The HOWSM is characterized by topological invariants for three-dimensional higher-order topological insulators, and the topological invariants are determined by the $C_4\mathcal{I}$-symmetry eigenvalues at the high-symmetry points. This HOWSM has chiral hinge modes as a direct consequence of the three-dimensional higher-order topology in the bulk.

DOI: 10.1103/PhysRevB.105.115119

I. INTRODUCTION

Higher-order topological insulators (HOTIs) have invoked paradigm shifts in condensed matter physics [1–8]. Two-dimensional (2D) HOTIs have corner modes localized at the corners of the systems, and three-dimensional (3D) HOTIs have corner modes or hinge modes localized at the intersections between the surfaces. Conventional n-dimensional topological insulators [9,10] have $(n-1)$-dimensional gapless states; namely, the gapless modes have codimension $d_c = 1$. In this case, the topological phases are classified as first-order topological phases. On the other hand, n-dimensional HOTIs have $(n-2)$- or $(n-3)$-dimensional gapless states. The former has codimension $d_c = 2$, and the latter has codimension $d_c = 3$, and therefore the former and the latter are second-order and third-order topological phases, respectively. Moreover, the coexistence of boundary modes with $d_c = m-1$ and those with $d_c = m$ has been studied in recent years and is referred to as hybrid-order topological phase [11–14].

Weyl semimetals (WSMs) [15–19] and Dirac semimetals [20–22] are topological phases with topologically protected gapless points in the bulk. WSMs have topological Fermi-arc surface states [23–26], and those with the boundary modes with codimension $d_c = 1$ are classified as the first-order topological phases. Recently, the concept of the higher-order topological phase (HOTP) was generalized to higher-order Dirac semimetals [27–33] and higher-order Weyl semimetals (HOWSMs) [34–41]. The HOWSM has both Fermi-arc surface states and hinge modes, and therefore it is classified as the hybrid-order topological phase.

Among various classes of HOTPs [42–58], some classes of 3D HOTIs have chiral hinge modes [1,2,4,7] akin to the edge modes of the 2D quantum Hall effect [59]. In addition, the HOTIs with chiral hinge modes protected by spatial symmetries are characterized by symmetry-based indicators [60–65]. For example, HOTIs with chiral hinge modes protected by inversion ($\mathcal{I}$) symmetry [66–69] can be characterized by a $\mathbb{Z}_4$ index in terms of the parity eigenvalues at high-symmetry points in the Brillouin zone (BZ) [65,70–72]. According to the classification of topological phases (key space groups) in Ref. [65], the chiral hinge modes detected by symmetry-based indicators are essentially limited to those protected by $\mathcal{I}$ symmetry and those protected by rotoinversion $C_4\mathcal{I}$ symmetry, where C_4 is a fourfold rotation symmetry. The chiral hinge modes protected by $\mathcal{I}$ symmetry have been explored in detail in Refs. [65–67,69,71,72], and the bulk-hinge correspondence for the HOTPs has been shown in Refs. [71,72]. Similarly, $C_4\mathcal{I}$-symmetric HOTPs have been studied in Refs. [7,73,74]. Nevertheless, they are based on $\boldsymbol{k}\cdot\boldsymbol{p}$ surface theory or the Wannier approach, and these approaches cannot be applied to some systems, as we discuss in Appendix A. Furthermore, the conventional discussions are insufficient in the following two points. First, the indicator does not explicitly appear in the discussions, and the role of the indicator is not clear in the bulk-hinge correspondence. Second, the discussions so far make use of certain properties of the models other than the indicator. Since the topological phase is characterized only by the indicator, its bulk-hinge correspondence should be explained by the indicator alone in principle. Thus, a general proof of the bulk-hinge correspondence characterized by the indicator has not been given.

In this paper, we show the bulk-hinge correspondence for HOTPs protected by $C_4\mathcal{I}$ symmetry. Our approach in this paper allows us to show the emergence of the chiral hinge modes only from the information of the $C_4\mathcal{I}$ symmetry eigenvalues at the high-symmetry points. In addition, we propose a class of the HOWSMs having chiral hinge modes protected by $C_4\mathcal{I}$ symmetry based on our theory of bulk-hinge correspondence. This HOWSM as a direct consequence of the 3D higher-order topology in the bulk is regarded as a generalization of the

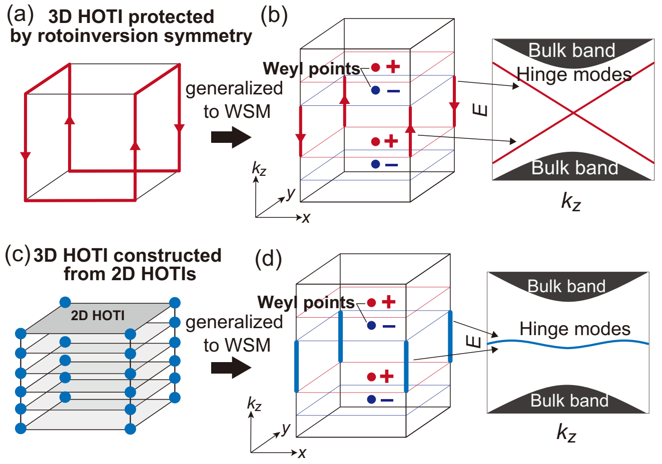

FIG. 1. Schematic drawings of HOTIs and HOWSMs. (a) 3D HOTIs protected by the rotoinversion symmetry. (b) HOWSMs with the chiral hinge modes originating from the 3D higher-order topology protected by the rotoinversion symmetry. Red and blue points represent monopoles and antimonopoles of Berry curvature, respectively. In this paper, we focus on this HOWSM with the hinge modes characterized by the topological invariants for 3D HOTIs. (c) 3D HOTIs constructed by stacking 2D HOTIs with corner modes. (d) HOWSMs studied in the previous works, where the hinge modes are not chiral.

3D HOTIs protected by $C_4\mathcal{I}$ symmetry [Figs. 1(a) and 1(b)]. Unlike the HOWSMs in the previous works [35,36], which are characterized by topological invariants for the 2D HOTI [Figs. 1(c) and 1(d)], the HOWSM in this paper has chiral hinge modes characterized by the topological invariants for 3D HOTIs. Because our HOWSM has Fermi-arc surface states and chiral hinge modes, it can be an ideal platform to study the interplay between first-order and second-order topology as the hybrid-order topological phase.

This paper is organized as follows. In Sec. II, we propose the HOWSM with the chiral hinge modes protected by $C_4\mathcal{I}$ symmetry in terms of a tight-binding model. In Sec. III, we show that the emergence of chiral hinge modes in insulators and WSMs with $C_4\mathcal{I}$ symmetry can be determined by the information of the $C_4\mathcal{I}$ symmetry eigenvalues. It is a proof of bulk-hinge correspondence for the HOTPs protected by $C_4\mathcal{I}$ symmetry. Conclusion and discussion are given in Sec. IV.

II. HIGHER-ORDER WEYL SEMIMETALS WITH CHIRAL HINGE MODES PROTECTED BY ROTOINVERSION SYMMETRY

In this section, we propose the concept of HOWSMs protected by $C_4\mathcal{I}$ symmetry based on a tight-binding model and demonstrate the bulk-hinge correspondence by numerical calculations. The proof of the bulk-hinge correspondence is given in Sec. III.

A. HOWSM protected by $C_{4z}\mathcal{I}$ symmetry

1. Topological invariants

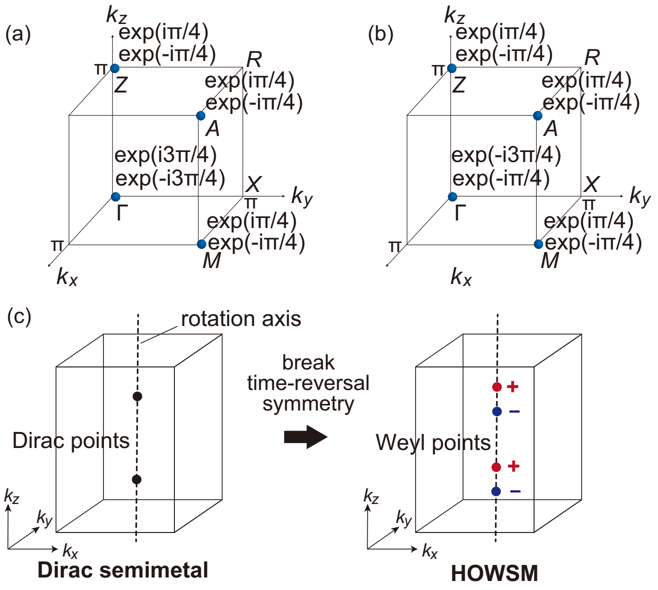

FIG. 2. (a, b) One-eighth of the BZ and examples of the $C_{4z}\mathcal{I}$-symmetry eigenvalues at the high-symmetry points. These $C_{4z}\mathcal{I}$-symmetry eigenvalues at the high-symmetry points satisfy (a) $\chi^{(+)}_{C_{4z}\mathcal{I}} = \chi^{(-)}_{C_{4z}\mathcal{I}} = 1$ and (b) $\chi^{(+)}_{C_{4z}\mathcal{I}} = 1$, $\chi^{(-)}_{C_{4z}\mathcal{I}} = 0$. (c) Phase transition from a C_4-symmetric Dirac semimetal to a HOWSM with $\chi^{(+)}_{C_{4z}\mathcal{I}} = \chi^{(-)}_{C_{4z}\mathcal{I}} = 1$. The HOWSM with $C_{4z}\mathcal{I}$ symmetry is obtained by adding a perturbation breaking $\mathcal{T}$ symmetry to the 3D Dirac semimetal. Because of $C_{4z}\mathcal{I}$ symmetry, the two Dirac points split to become the two pairs of the Weyl points on the rotation axis.

Here, we discuss topological invariants for the HOTPs protected by $C_{4z}\mathcal{I}$, where C_{4z} is a fourfold rotational symmetry about the z axis. The operation $C_{4z}\mathcal{I}$ changes wave vectors as $(k_x, k_y, k_z) \rightarrow (k_y, -k_x, -k_z)$. Therefore, this system has four $C_{4z}\mathcal{I}$-invariant points in the k-space: $K_4 = \{\Gamma = (0,0,0),\ \ M = (\pi,\pi,0),\ \ Z = (0,0,\pi),\ \ A = (\pi,\pi,\pi)\}$. Figure 2(a) shows 1/8 of the 3D BZ and the high-symmetry points. To capture the HOTPs protected by $C_{4z}\mathcal{I}$ symmetry, let us introduce the following indices in terms of the numbers of occupied states with symmetry eigenvalues at K_4:

$$\begin{aligned}\chi^{(\pm)}_{C_{4z}\mathcal{I}} \equiv \tfrac{1}{2}\big[&n_{\pm\frac{\pi}{4}}(Z) - n_{\mp\frac{3\pi}{4}}(Z) + n_{\pm\frac{\pi}{4}}(A)\\ &- n_{\mp\frac{3\pi}{4}}(A) - n_{\pm\frac{\pi}{4}}(\Gamma) + n_{\mp\frac{3\pi}{4}}(\Gamma)\\ &- n_{\pm\frac{\pi}{4}}(M) + n_{\mp\frac{3\pi}{4}}(M)\big] \bmod 2,\end{aligned} \qquad (1)$$

where $n_{+\frac{\pi}{4}}(\boldsymbol{k})$, $n_{-\frac{\pi}{4}}(\boldsymbol{k})$, $n_{+\frac{3\pi}{4}}(\boldsymbol{k})$, and $n_{-\frac{3\pi}{4}}(\boldsymbol{k})$ are the numbers of occupied states with $C_{4z}\mathcal{I}$ eigenvalues $e^{+i\frac{\pi}{4}}$, $e^{-i\frac{\pi}{4}}$, $e^{+i\frac{3\pi}{4}}$, and $e^{-i\frac{3\pi}{4}}$ at the $C_{4z}\mathcal{I}$-invariant wave vector $\boldsymbol{k}$, respectively. Here we assume that the Chern numbers at $k_z = 0$ and $k_z = \pi$ are zero. This ensures that $\chi^{(\pm)}_{C_{4z}\mathcal{I}}$ are integers. When the Chern numbers are nonzero, the hinge modes will be hidden by chiral surface states due to a nonzero Chern number. In this paper, to study the hinge modes, we restrict ourselves to systems with the Chern numbers at $k_z = 0$ and $k_z = \pi$ being zero. The topological invariants $\chi^{(\pm)}_{C_{4z}\mathcal{I}}$ can be defined both for insulators and for WSMs when the bulk and the surfaces of the WSMs are gapped at $k_z = 0$ and $k_z = \pi$. Figures 2(a) and 2(b) show two examples of the $C_{4z}\mathcal{I}$-symmetry eigenvalues at the high-symmetry points satisfying $\chi^{(+)}_{C_{4z}\mathcal{I}} = \chi^{(-)}_{C_{4z}\mathcal{I}} = 1$ and $\chi^{(+)}_{C_{4z}\mathcal{I}} = 1$, $\chi^{(-)}_{C_{4z}\mathcal{I}} = 0$, respectively. In Sec. III, we will show that when $\chi^{(+)}_{C_{4z}\mathcal{I}} \equiv \chi^{(-)}_{C_{4z}\mathcal{I}} \equiv 1 \bmod 2$, chiral hinge modes appear in insulators or WSMs.

2. Phase transition for the HOWSM

Now we discuss how to construct a HOWSM protected by $C_{4z}\mathcal{I}$ symmetry. The HOWSM can be realized by adding a perturbation breaking time-reversal ($\mathcal{T}$) symmetry to a 3D nonmagnetic Dirac semimetal with C_{4z} symmetry. We start with a 3D Dirac semimetal with two fourfold-degenerate points (Dirac points) on the rotation axis [Fig. 2(c)]. Then, we perturb it to split each Dirac point into a pair of Weyl points on the rotation axis while preserving $C_{4z}\mathcal{I}$ symmetry. The topological phase transition for the HOWSM can be induced by magnetic doping or an external magnetic field [20,75] without breaking $C_{4z}\mathcal{I}$ symmetry in the Dirac semimetals.

3. Tight-binding model of the HOWSM

According to the above discussion, we introduce a spinful tight-binding model of a HOWSM with $\chi^{(+)}_{C_{4z}\mathcal{I}} \equiv 1$ and $\chi^{(-)}_{C_{4z}\mathcal{I}} \equiv 1 \bmod 2$. This tight-binding model is defined on the simple tetragonal lattice, and each site has four orbitals. In the following, we set the lattice constants to 1. The Hamiltonian is given by

$$\mathcal{H}(\boldsymbol{k}) = \mathcal{H}_{\mathrm{DSM}}(\boldsymbol{k}) + \mathcal{H}_{C_{4z}\mathcal{I}}(\boldsymbol{k}) + \mathcal{H}_{z}(\boldsymbol{k}), \tag{2}$$

with

$$\begin{aligned}\mathcal{H}_{\mathrm{DSM}}(\boldsymbol{k}) \equiv & \left(-m + c \sum_{j=x,y,z} \cos k_j\right)\sigma_0\tau_z \\ & - v\left(\sum_{j=x,y} \sin k_j \sigma_j\right)\tau_x,\end{aligned} \tag{3}$$

$$\mathcal{H}_{C_{4z}\mathcal{I}}(\boldsymbol{k}) \equiv v_s(\cos k_x - \cos k_y)\sigma_0\tau_x + v_t(\cos k_x - \cos k_y)\sigma_0\tau_y, \tag{4}$$

$$\mathcal{H}_{z}(\boldsymbol{k}) \equiv v_z \sin k_z \sigma_z \tau_x + B_z \sigma_z \tau_0, \tag{5}$$

where σ_j, τ_j ($j = x, y, z$) are the Pauli matrices corresponding to the spin and the orbital degrees of freedom, respectively, and σ_0, τ_0 are the 2×2 identity matrices. $\mathcal{H}_{\mathrm{DSM}}(\boldsymbol{k})$ is a model for a 3D Dirac semimetal with $\mathcal{T}$ symmetry, where $\mathcal{T}$ can be expressed as $\mathcal{T} = -i\sigma_y\tau_0 K$ with K being the complex conjugation. On the other hand, the second term of $\mathcal{H}_{C_{4z}\mathcal{I}}(\boldsymbol{k})$ breaks $\mathcal{T}$ symmetry. In addition, $\mathcal{H}_z(\boldsymbol{k})$ makes the Dirac points of $\mathcal{H}_{\mathrm{DSM}}(\boldsymbol{k})$ split into Weyl points.

The overall Hamiltonian has $C_{4z}\mathcal{I}$ symmetry,

$$C_{4z}\mathcal{I}\mathcal{H}(k_x, k_y, k_z)(C_{4z}\mathcal{I})^{-1} = \mathcal{H}(k_y, -k_x, -k_z), \tag{6}$$

where $C_{4z}\mathcal{I} = e^{-i\frac{\pi}{4}\sigma_z}\tau_z$. This Hamiltonian does not have $C_{4z}\mathcal{T}$ symmetry because the first term of $\mathcal{H}_{C_{4z}\mathcal{I}}(\boldsymbol{k})$ breaks it. Therefore, the topological phases of this Hamiltonian cannot be characterized by a topological invariant protected by $C_{4z}\mathcal{T}$ symmetry [7]. Instead, we need to use the topological invariant $\chi^{(\pm)}_{C_{4z}\mathcal{I}}$ to analyze the topological phases in this model. In the following, we set the parameters as $m = 4$, $c = 2$, $v = 1$, $v_z = 0.2$, $v_s = 0.4$, $v_t = 1$, and $B_z = 1$, and we set the Fermi energy to be zero. In this model with these parameters, the $C_{4z}\mathcal{I}$ eigenvalues of occupied states at the high-symmetry points are shown in Fig. 2(a), and therefore the numbers of $C_{4z}\mathcal{I}$ eigenvalues at high-symmetry points satisfy $\chi^{(+)}_{C_{4z}\mathcal{I}} = \chi^{(-)}_{C_{4z}\mathcal{I}} = 1$. In the following, we perform calculations of the tight-binding model using the PYTHTB package [76]. Figure 3(a) shows a bulk band structure of the tight-binding model [Eq. (2)]. In Fig. 3(a), Weyl points appear between Γ and Z in the k-space.

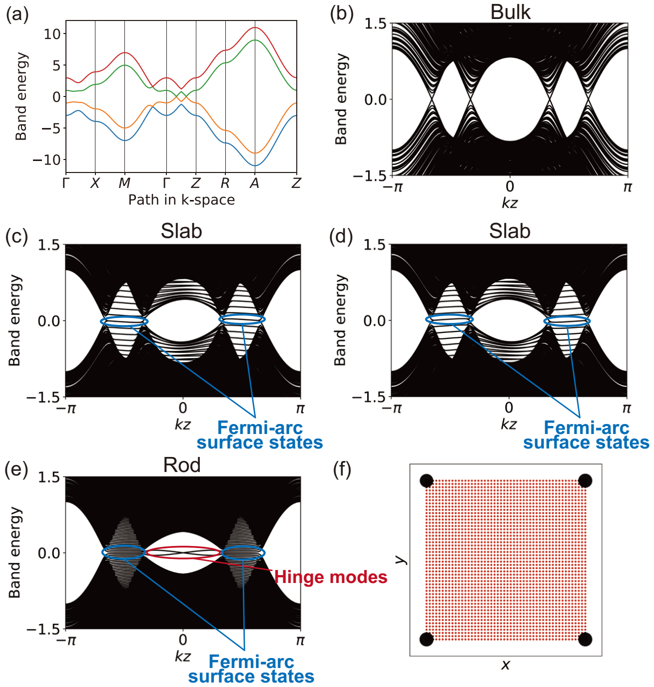

FIG. 3. (a) Bulk band structure of the tight-binding model of Eq. (2). (b–e) The band structures with the system size being $L_x \times L_y = 50 \times 50$ in the x and $y$directions. The band structures with (b) the periodic boundary conditions in the x and y directions, (c) the open boundary condition in the x direction and the periodic boundary condition in the y direction, (d) the periodic boundary condition in the x direction and the open boundary condition in the y direction, and (e) the open boundary conditions in the x and y directions. (f) The real-space distribution of zero-energy modes of (e).

Next, to see behaviors of the hinge modes and the surface states of our model, we calculate band structures in the bulk, in the slab, and in the rod geometries, and compare them. Figures 3(b)–3(e) show the band structures with these different geometries. The system has surfaces in both Fig. 3(c) and Fig. 3(d), and the Fermi-arc surface states appear in these cases. In Fig. 3(e), the system has surfaces and hinges, resulting in the emergence of the hinge modes. While the Fermi-arc surface states exist here, the surface states have a minigap in Fig. 3(e) because of the finite-size effects.

From the model calculations, we have found several features of the HOWSM protected by $C_{4z}\mathcal{I}$ symmetry. The Fermi-arc surface states appear when the system has the open boundary condition in one direction, and the chiral hinge modes appear only when the system has the open boundary conditions in the two directions. The chiral hinge modes of the HOWSM are localized at the four corners in the real space [see Fig. 3(f)] because of $C_{4z}\mathcal{I}$ symmetry.

As a comparison with this $C_{4z}\mathcal{I}$-symmetric HOWSM, we calculate a tight-binding model of a HOWSM protected by $\mathcal{I}$ symmetry in Appendix B. The calculations in Appendix B show that the chiral hinge modes of the $\mathcal{I}$-symmetric HOWSM appear at two corners facing in opposite directions in the real space. Therefore, the localizations of the hinge modes at the four corners are the characteristic of the $C_{4z}\mathcal{I}$-symmetric HOWSM. As we discuss in Appendix C, the chiral hinge modes are limited to $\mathcal{I}$-symmetric ones and $C_{4z}\mathcal{I}$-symmetric ones in type-I magnetic space groups. Thus, we exhaust all possible phases of HOWSMs with chiral hinge modes in type-I magnetic space groups.

B. Topological invariants for insulators with $C_{4z}\mathcal{I}$ symmetry

So far we mainly discussed HOWSMs with $C_{4z}\mathcal{I}$ symmetry. In this section, we discuss the topological invariants for insulators with $C_{4z}\mathcal{I}$ symmetry. For insulators, we can greatly simplify our indices $\chi^{(\pm)}_{C_{4z}\mathcal{I}}$ and connect them to the symmetry-based indicators in insulators [60–63,65,77] by considering the twofold rotation (C_{2z}) symmetry about the z axis because $C_{2z}=(C_{4z}\mathcal{I})^2$. Let $n^{(+\frac{\pi}{2})}_{C_{2z}}(\boldsymbol{k})$ and $n^{(-\frac{\pi}{2})}_{C_{2z}}(\boldsymbol{k})$ denote the number of occupied states with the $+i$ and $-i$ eigenvalues of the C_{2z} symmetry at high-symmetry points, respectively. C_{2z} symmetry is preserved on the high-symmetry lines Γ-Z and M-A, and therefore in insulators, the numbers of occupied bands with the $+i$ and $-i$ eigenvalues of the C_{2z} symmetry do not change along these lines:

$$n^{(+\frac{\pi}{2})}_{C_{2z}}(\Gamma)=n^{(+\frac{\pi}{2})}_{C_{2z}}(Z),\ n^{(-\frac{\pi}{2})}_{C_{2z}}(\Gamma)=n^{(-\frac{\pi}{2})}_{C_{2z}}(Z), \tag{7}$$

$$n^{(+\frac{\pi}{2})}_{C_{2z}}(M)=n^{(+\frac{\pi}{2})}_{C_{2z}}(A),\ n^{(-\frac{\pi}{2})}_{C_{2z}}(M)=n^{(-\frac{\pi}{2})}_{C_{2z}}(A). \tag{8}$$

Such restrictions for the numbers of occupied states with the symmetry eigenvalues at high-symmetry points are referred to as compatibility relations. The compatibility relations hold in any band insulators.

The states with the $e^{i\frac{\pi}{4}}$ and $e^{-i\frac{3\pi}{4}}$ eigenvalues of $C_{4z}\mathcal{I}$ symmetry have the $+i$ eigenvalue of C_{2z} symmetry. Thus, Eq. (7) and Eq. (8) can be expressed as

$$n_{+\frac{\pi}{4}}(Z)+n_{-\frac{3\pi}{4}}(Z)=n_{+\frac{\pi}{4}}(\Gamma)+n_{-\frac{3\pi}{4}}(\Gamma), \tag{9}$$

$$n_{+\frac{\pi}{4}}(A)+n_{-\frac{3\pi}{4}}(A)=n_{+\frac{\pi}{4}}(M)+n_{-\frac{3\pi}{4}}(M). \tag{10}$$

By combining Eqs. (1), (9), and (10), we can rewrite our index $\chi^{(+)}_{C_{4z}\mathcal{I}}$ as

$$\begin{aligned}\chi^{(+)}_{C_{4z}\mathcal{I}}&\equiv n_{+\frac{\pi}{4}}(Z)-n_{+\frac{\pi}{4}}(\Gamma)+n_{+\frac{\pi}{4}}(A)-n_{+\frac{\pi}{4}}(M)\\&\equiv\sum_{\Gamma_i\in K_4}n_{+\frac{\pi}{4}}(\Gamma_i)\ \bmod 2.\end{aligned} \tag{11}$$

Similarly, the compatibility relations for the $-i$ eigenvalue of C_{2z} symmetry allow us to rewrite our index $\chi^{(-)}_{C_{4z}\mathcal{I}}$ as

$$\chi^{(-)}_{C_{4z}\mathcal{I}}\equiv\sum_{\Gamma_i\in K_4}n_{-\frac{\pi}{4}}(\Gamma_i)\ \bmod 2. \tag{12}$$

In addition, as we show in Appendix D, the difference between the Chern numbers on $k_z=0$ and $k_z=\pi$ is given by

$$\mathrm{Ch}|_{k_z=0}-\mathrm{Ch}|_{k_z=\pi}\equiv 2\left(\chi^{(+)}_{C_{4z}\mathcal{I}}+\chi^{(-)}_{C_{4z}\mathcal{I}}\right)\ \bmod 4. \tag{13}$$

Therefore, when one of our indices $\chi^{(\pm)}_{C_{4z}\mathcal{I}}$ is an odd number and the other is an even number, the value of Eq. (13) is equal to 2 mod 4, and the system has a nontrivial Chern number on $k_z=0$ or $k_z=\pi$.

The space group generated by $C_{4z}\mathcal{I}$ is No. 81 ($P\bar{4}$). Because we do not assume $\mathcal{T}$ symmetry, it is the type-I magnetic space group No. 81.33 generated by $C_{4z}\mathcal{I}$. Its symmetry-based indicators are given by $\mathbb{Z}_2\times\mathbb{Z}_2\times\mathbb{Z}_4$ [63]. The $\mathbb{Z}_4$ index corresponds to a weak index being equal to the Chern number $\mathrm{Ch}|_{k_z=0}$ mod 4. The first $\mathbb{Z}_2$ index is a strong index to detect whether the number of Weyl points in $0\leqslant k_z\leqslant\pi$ is $4n$ or $4n+2$ ($n=$ integer). It is equal to the difference of the Chern numbers between $k_z=0$ and $k_z=\pi$ [65,77,78]. Therefore, this $\mathbb{Z}_2$ index is equal to the parity of $\chi^{(+)}_{C_{4z}\mathcal{I}}+\chi^{(-)}_{C_{4z}\mathcal{I}}$ from Eq. (13). In this paper, we focus on the system with the Chern numbers on $k_z=0$ and $k_z=\pi$ being zero. This assumption leads to $\chi^{(+)}_{C_{4z}\mathcal{I}}+\chi^{(-)}_{C_{4z}\mathcal{I}}\equiv 0$ mod 2. This allows two possibilities: $\chi^{(+)}_{C_{4z}\mathcal{I}}\equiv\chi^{(-)}_{C_{4z}\mathcal{I}}\equiv 0$ or 1 mod 2. They are distinguished in terms of the second $\mathbb{Z}_2$ index. Namely, when $\chi^{(+)}_{C_{4z}\mathcal{I}}\equiv\chi^{(-)}_{C_{4z}\mathcal{I}}\equiv 1$ mod 2, the second $\mathbb{Z}_2$ is equal to $\mathbb{Z}_2=1$, and it is the HOTPs protected by $C_{4z}\mathcal{I}$ symmetry. In this way, our indices match with the symmetry-based indicators in the previous works.

In the previous work [65,78], a quantity μ_4 defined by

$$\mu_4=\frac{1}{\sqrt{2}}\sum_{\Gamma_i\in K_4}\sum_{\alpha}e^{i\alpha}n_\alpha(\Gamma_i) \tag{14}$$

is proposed as a symmetry-based indicator in the magnetic space group No. 81.33, where α runs over $\alpha=\pm\pi/4,\pm3\pi/4$. According to Refs. [65,78], $\mu_4=2$ or $\mu_4=2i$ correspond to nontrivial phases. Furthermore, in the previous work [77], the symmetry-based indicator is given by

$$z_2\equiv\frac{1}{2}\sum_{\Gamma_i\in K_4}\left(n_{-\frac{\pi}{4}}(\Gamma_i)-n_{+\frac{3\pi}{4}}(\Gamma_i)\right)\ \bmod 2 \tag{15}$$

in the magnetic space group No. 81.33. According to Ref. [77], $z_2=1$ corresponds to nontrivial phases. When the Chern numbers at $k_z=0$ and π are zero, both $\mu_4=2, 2i$ and $z_2=1$ are equivalent to $\chi^{(+)}_{C_{4z}\mathcal{I}}\equiv\chi^{(-)}_{C_{4z}\mathcal{I}}\equiv 1$ mod 2. While the indices $\chi^{(\pm)}_{C_{4z}\mathcal{I}}$ detect the same HOTP as the symmetry-based indicators μ_4 and z_2, we propose the indices $\chi^{(\pm)}_{C_{4z}\mathcal{I}}$ in this paper to be the useful indices to detect the HOTP protected by $C_{4z}\mathcal{I}$ symmetry from the discussions of spectral flows in Sec. III. In contrast, the formula of the symmetry-based indicator μ_4 and z_2 may not have a direct physical interpretation.

III. BULK-HINGE CORRESPONDENCE FOR HIGHER-ORDER TOPOLOGICAL PHASES

In this section, we show the bulk-hinge correspondence for HOTPs in insulators and WSMs with $C_{4z}\mathcal{I}$ symmetry only from the $C_{4z}\mathcal{I}$ eigenvalues at the high-symmetry points in the BZ. From this bulk-hinge correspondence, we can confirm that the chiral hinge modes of our model in the previous section originate from the nontrivial indices $\chi^{(\pm)}_{C_{4z}\mathcal{I}}$ introduced in the previous section. In the following discussion, we show that when our indices $\chi^{(\pm)}_{C_{4z}\mathcal{I}}$ [see Eq. (1)] satisfy $\chi^{(+)}_{C_{4z}\mathcal{I}}\equiv\chi^{(-)}_{C_{4z}\mathcal{I}}\equiv 1$ mod 2, the chiral hinge modes appear.

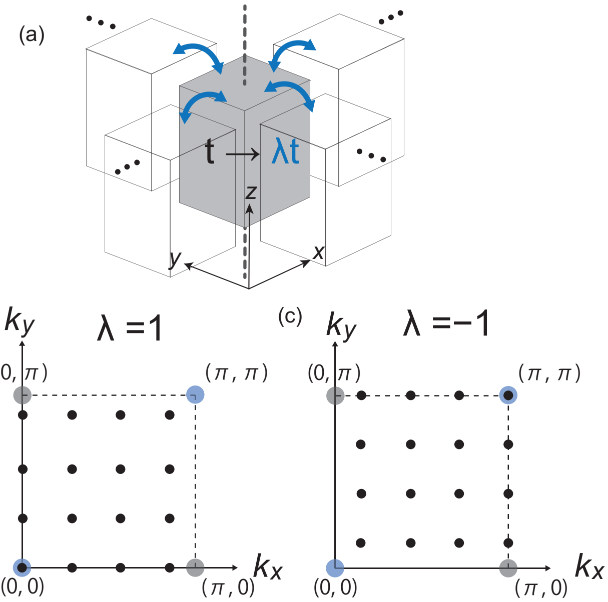

FIG. 4. Cutting procedures and boundary conditions. (a) Geometry of the system with boundary conditions controlled by a cutting parameter λ with the finite system size $L_x \times L_y$ in the x and y directions. (b) Possible wave vectors (k_x, k_y) with $\lambda = 1$. Black dots represent the possible wave vectors. $\lambda = 1$ leads to the periodic boundary conditions in the x and y directions and the the wave vectors $k_i = \frac{2\pi}{L_i} m_i$ $(-M \leqslant m_i \leqslant M)$ $(i = x, y)$. (c) Possible wave vectors (k_x, k_y) with $\lambda = -1$. $\lambda = -1$ leads to the antiperiodic boundary conditions in the x and y directions and the wave vectors $k_i = \frac{2\pi}{L_i} m_i + \frac{\pi}{L_i}$ $(-M \leqslant m_i \leqslant M)$ $(i = x, y)$.

A. Setup of the problem

Here, we consider a general 3D spinful electronic system with $C_{4z}\mathcal{I}$ symmetry. In addition, we assume that the system is an insulator and a WSM with the bulk being gapped at $k_z = 0$ and $k_z = \pi$. We do not assume $\mathcal{T}$ symmetry. In the following discussion, we assume that the surfaces are gapped at $k_z = 0$ and $k_z = \pi$ in the system with finite sizes in the x and y directions. Here, we consider a large but finite system in the x and y directions with the system size $L_x \times L_y = (2M + 1) \times (2M + 1)$ (where M is an integer), where the length of the system is measured in the unit of the lattice constant. The lattice sites (x, y) with $x, y \in \mathbb{Z}$ satisfy $-M \leqslant x \leqslant M$ and $-M \leqslant y \leqslant M$. Furthermore, we set the system size L_z along the z direction as $L_z \to \infty$ and electronic states are labeled by the wave number k_z along the z direction.

Next, we introduce hoppings between sites $x = -M$ and $x = M$ in the similar way as in the bulk but all the hopping amplitudes between $x = -M$ and $x = M$ are multiplied by a real parameter λ. Similarly, we introduce the hoppings between the sites $y = -M$ and $y = M$ multiplied by λ. For example, when the bulk Hamiltonian has a hopping parameter t in the x (y) direction, the hoppings between $x = -M$ and $x = M$ ($y = -M$ and $y = M$) are given by λt [Fig. 4(a)]. The system has two parameters, k_z and λ, and we write the Hamiltonian of the system as $\mathcal{H}(k_z, \lambda)$. The Hamiltonian $\mathcal{H}(k_z, \lambda)$ has periodic boundary conditions in the x and y directions when $\lambda = 1$, while it has open boundary conditions in the x and y directions when $\lambda = 0$.

The Hamiltonian $\mathcal{H}(k_z, \lambda)$ has C_{2z} symmetry because $(C_{4z}\mathcal{I})^2 = C_{2z}$:

$$C_{2z}\mathcal{H}(k_z, \lambda)C_{2z}^{-1} = \mathcal{H}(k_z, \lambda). \tag{16}$$

Therefore, under an appropriate unitary transformation U, $\mathcal{H}(k_z, \lambda)$ can be transformed into the following direct sum of (+) and (−) sectors labeled by the $+i$ and $-i$ eigenvalues of C_{2z}, respectively:

$$U\mathcal{H}(k_z, \lambda)U^\dagger = \tilde{\mathcal{H}}(k_z, \lambda) = \begin{pmatrix} \mathcal{H}^{(+)}(k_z, \lambda) & 0 \\ 0 & \mathcal{H}^{(-)}(k_z, \lambda) \end{pmatrix}. \tag{17}$$

Then we define the total numbers of occupied states with $C_{4z}\mathcal{I}$ eigenvalues $e^{i\frac{\pi}{4}}$, $e^{-i\frac{\pi}{4}}$, $e^{i\frac{3\pi}{4}}$, and $e^{-i\frac{3\pi}{4}}$ as $N_{+\frac{\pi}{4}}(k_z, \lambda)$, $N_{-\frac{\pi}{4}}(k_z, \lambda)$, $N_{+\frac{3\pi}{4}}(k_z, \lambda)$, and $N_{-\frac{3\pi}{4}}(k_z, \lambda)$, respectively. In addition, for the following discussions, we introduce the following integers from the numbers of occupied states with $C_{4z}\mathcal{I}$ eigenvalues:

$$\mathcal{N}^{(\pm)}_{C_{4z}\mathcal{I}}(k_z)|_\lambda \equiv N_{\pm\frac{\pi}{4}}(k_z, \lambda) - N_{\mp\frac{3\pi}{4}}(k_z, \lambda). \tag{18}$$

The square of $e^{i\frac{\pi}{4}}$ and the square of $e^{-i\frac{3\pi}{4}}$ are $+i$, and the square of $e^{-i\frac{\pi}{4}}$ and the square of $e^{i\frac{3\pi}{4}}$ are $-i$. Thus, (±) labels of $\mathcal{N}^{(\pm)}_{C_{4z}\mathcal{I}}(k_z)|_\lambda$ correspond to the (±) sectors of the Hamiltonian $\mathcal{H}^{(+)}(k_z, \lambda)$ and $\mathcal{H}^{(-)}(k_z, \lambda)$.

B. Cutting procedures and spectral flows

Here, we show the bulk-hinge correspondence with $C_{4z}\mathcal{I}$ symmetry by considering changes in the energy spectra through changing the cutting parameter. When the cutting parameter is $\lambda = 1$, the wave vectors in the x and y directions are $k_i = \frac{2\pi}{L_i} m_i$ $(-M \leqslant m_i \leqslant M)$ $(i = x, y)$ because of the periodic boundary condition in the x and y directions. On the other hand, in the case with $\lambda = -1$, the wave vectors are given by $k_i = \frac{2\pi}{L_i} m_i + \frac{\pi}{L_i}$ $(-M \leqslant m_i \leqslant M)$ $(i = x, y)$ because of the antiperiodic boundary condition. The proof of this is given in Appendix E 1. We note that here k_x and k_y are well defined only for $\lambda = \pm 1$ because of the periodic boundary conditions ($\lambda = 1$) and the antiperiodic boundary conditions ($\lambda = -1$) [see Figs. 4(b) and 4(c)]. For both the cases with $\lambda = 1$ and $\lambda = -1$, each wave function ψ_m at non-$C_{4z}\mathcal{I}$-symmetric momenta $\boldsymbol{k}$ with $k_z = 0$ or π can always be mixed with the wave functions at $\hat{C}_{4z}\hat{\mathcal{I}}\boldsymbol{k}$, $(\hat{C}_{4z}\hat{\mathcal{I}})^2\boldsymbol{k}$, and $(\hat{C}_{4z}\hat{\mathcal{I}})^3\boldsymbol{k}$ to construct four eigenstates of $C_{4z}\mathcal{I}$:

$$|\phi_\alpha\rangle \equiv |\psi_m(\boldsymbol{k})\rangle + e^{-i\alpha}\hat{C}_{4z}\hat{\mathcal{I}}\,|\psi_m(\boldsymbol{k})\rangle + e^{-2i\alpha}(\hat{C}_{4z}\hat{\mathcal{I}})^2\,|\psi_m(\boldsymbol{k})\rangle + e^{-3i\alpha}(\hat{C}_{4z}\hat{\mathcal{I}})^3\,|\psi_m(\boldsymbol{k})\rangle\,, \tag{19}$$

$$\hat{C}_{4z}\hat{\mathcal{I}}\,|\phi_\alpha\rangle = e^{i\alpha}\,|\phi_\alpha\rangle\,, \tag{20}$$

where $\alpha = \pm\frac{\pi}{4}, \pm\frac{3\pi}{4}$. Therefore, states at non-$C_{4z}\mathcal{I}$-symmetric points do not contribute to $\mathcal{N}^{(\pm)}_{C_{4z}\mathcal{I}}$.

On the other hand, the states at $C_{4z}\mathcal{I}$-symmetric momenta contribute to $\mathcal{N}^{(\pm)}_{C_{4z}\mathcal{I}}(k_z)|_\lambda$. When $\lambda = 1$, the wave vector (k_x, k_y) can take a value (0,0), but not (π, π) [Fig. 4(b)]. When $\lambda = -1$, the wave vector (k_x, k_y) can take a value (π, π), but not (0,0) [Fig. 4(c)]. Therefore, $\mathcal{N}^{(\pm)}_{C_{4z}\mathcal{I}}(k_z)|_{\lambda=\pm1}$ is determined by the number of occupied states with the $C_{4z}\mathcal{I}$

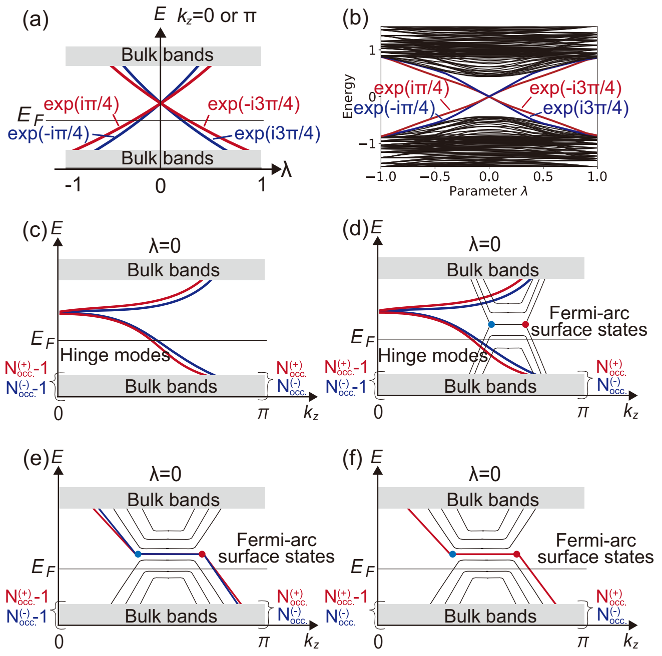

FIG. 5. Spectral flows in the band gaps and the emergence of hinge modes. The spectral flows in the sectors labeled by the (+) and (−) eigenvalues of C_{2z} are red and blue lines, respectively. (a) The changes of the energy spectra in changing λ from λ = −1 to λ = 1 with $k_z = 0$ or π. (b) Spectral flows of the tight-binding model of Eq. (2) in the process of changing λ from λ = −1 to λ = 1. (c) Emergence of chiral hinge modes between $k_z = 0$ and $k_z = \pi$ in insulators. The numbers of occupied bands in the (±) sectors labeled by the C_{2z} eigenvalues satisfy $\nu^{(\pm)}(k_z = 0) = N^{(\pm)}_{\text{occ.}} - 1$ and $\nu^{(\pm)}(k_z = \pi) = N^{(\pm)}_{\text{occ.}}$. (d) Emergence of chiral hinge modes between $k_z = 0$ and $k_z = \pi$ in WSMs with $\chi^{(+)}_{C_{4z}\mathcal{I}} \equiv \chi^{(-)}_{C_{4z}\mathcal{I}} \equiv 1 \bmod 2$. (e) Emergence of Fermi-arc surface states in WSMs with $\chi^{(+)}_{C_{4z}\mathcal{I}} \equiv \chi^{(-)}_{C_{4z}\mathcal{I}} \equiv 1 \bmod 2$. (f) Emergence of Fermi-arc surface states with $\chi^{(+)}_{C_{4z}\mathcal{I}} \equiv 1 \bmod 2$ and $\chi^{(-)}_{C_{4z}\mathcal{I}} \equiv 0 \bmod 2$.

eigenvalues at $\boldsymbol{k}$:

$$\mathcal{N}^{(\pm)}_{C_{4z}\mathcal{I}}(0)|_{\lambda=1} = n_{\pm\frac{\pi}{4}}(\Gamma) - n_{\mp\frac{3\pi}{4}}(\Gamma),$$

$$\mathcal{N}^{(\pm)}_{C_{4z}\mathcal{I}}(0)|_{\lambda=-1} = n_{\pm\frac{\pi}{4}}(M) - n_{\mp\frac{3\pi}{4}}(M),$$

$$\mathcal{N}^{(\pm)}_{C_{4z}\mathcal{I}}(\pi)|_{\lambda=1} = n_{\pm\frac{\pi}{4}}(Z) - n_{\mp\frac{3\pi}{4}}(Z),$$

$$\mathcal{N}^{(\pm)}_{C_{4z}\mathcal{I}}(\pi)|_{\lambda=-1} = n_{\pm\frac{\pi}{4}}(A) - n_{\mp\frac{3\pi}{4}}(A), \tag{21}$$

where Γ, M, Z, and A are the high-symmetry points in the BZ defined in Sec. II A [see Fig. 2(a)].

Next, we discuss changes of the band structures while continuously changing the parameter λ from λ = −1 to λ = 1. We call these changes of the band energy in this process "spectral flows." When the bulk and the surfaces are gapped at $k_z = 0$ and π and M is sufficiently large, the spectral flows in the band gap have the following important properties:

(i) The spectral flows in the band gap are symmetric under λ ↔ −λ, namely, $E(k_z, \lambda) = E(k_z, -\lambda)$ [Fig. 5(a)].

(ii) When a state with the energy $E(k_z, \lambda)$ has the $e^{i\alpha}$ eigenvalue of $C_{4z}\mathcal{I}$ ($\alpha = \pm\pi/4, \pm 3\pi/4$), a state with the energy $E(k_z, -\lambda)$ has the $-e^{i\alpha}$ eigenvalue [Fig. 5(a)].

The proofs of these properties (i) and (ii) of the spectral flows are given in Appendices E 2 and E 3, respectively. From properties (i) and (ii), we find that when $N_{+\frac{\pi}{4}}(k_z, \lambda)$ decreases by an integer N in changing λ from λ = −1 to λ = 0, $N_{-\frac{3\pi}{4}}(k_z, \lambda)$ increases by N in changing λ from λ = 0 to λ = 1. Similarly, when $N_{-\frac{\pi}{4}}(k_z, \lambda)$ decreases by N in changing λ from λ = −1 to λ = 0, $N_{+\frac{3\pi}{4}}(k_z, \lambda)$ increases by N in changing λ from λ = 0 to λ = 1. In this way, properties (i) and (ii) restrict changes of $N_{+\frac{\pi}{4}}(k_z, \lambda)$, $N_{-\frac{\pi}{4}}(k_z, \lambda)$, $N_{+\frac{3\pi}{4}}(k_z, \lambda)$, and $N_{-\frac{3\pi}{4}}(k_z, \lambda)$ through the cutting procedure. Therefore, the changes of $\mathcal{N}^{(\pm)}_{C_{4z}\mathcal{I}}(k_z)|_\lambda$ from λ = −1 to λ = 0 are equal to the changes of $\mathcal{N}^{(\pm)}_{C_{4z}\mathcal{I}}(k_z)|_\lambda$ from λ = 0 to λ = 1:

$$\begin{aligned}&\mathcal{N}^{(\pm)}_{C_{4z}\mathcal{I}}(k_z)|_{\lambda=1} - \mathcal{N}^{(\pm)}_{C_{4z}\mathcal{I}}(k_z)|_{\lambda=0}\\ &\quad = \mathcal{N}^{(\pm)}_{C_{4z}\mathcal{I}}(k_z)|_{\lambda=0} - \mathcal{N}^{(\pm)}_{C_{4z}\mathcal{I}}(k_z)|_{\lambda=-1}.\end{aligned} \tag{22}$$

By combining Eqs. (21) and (22), we obtain the following equations:

$$\begin{aligned}\mathcal{N}^{(\pm)}_{C_{4z}\mathcal{I}}(0)|_{\lambda=0} = &\frac{1}{2}\left(n_{\pm\frac{\pi}{4}}(\Gamma) - n_{\mp\frac{3\pi}{4}}(\Gamma)\right)\\ &+ \frac{1}{2}\left(n_{\pm\frac{\pi}{4}}(M) - n_{\mp\frac{3\pi}{4}}(M)\right),\end{aligned} \tag{23}$$

$$\begin{aligned}\mathcal{N}^{(\pm)}_{C_{4z}\mathcal{I}}(\pi)|_{\lambda=0} = &\frac{1}{2}\left(n_{\pm\frac{\pi}{4}}(Z) - n_{\mp\frac{3\pi}{4}}(Z)\right)\\ &+ \frac{1}{2}\left(n_{\pm\frac{\pi}{4}}(A) - n_{\mp\frac{3\pi}{4}}(A)\right).\end{aligned} \tag{24}$$

In addition, to confirm that our theory is consistent with the previous section, we calculate the spectral flows of our model [Eq. (2)] in the cutting procedure with $L_x \times L_y = 15 \times 15$, and the periodic boundary condition in the z direction. Figure 5(b) shows the spectral flows through changing the cutting parameter λ from λ = −1 to λ = 1 with $k_z = 0$. In changing λ from λ = −1 to λ = 1, occupied states with the eigenvalues $e^{i\frac{\pi}{4}}$ and $e^{-i\frac{\pi}{4}}$ move to conduction bands, while unoccupied states with the eigenvalues $e^{i\frac{3\pi}{4}}$ and $e^{-i\frac{3\pi}{4}}$ move to valence bands, which perfectly agrees with the above discussion [Fig. 5(a)].

To see behaviors of hinge modes, we introduce $\nu^{(\pm)}(k_z)$ as the total numbers of occupied states of $\mathcal{H}^{(\pm)}(k_z, \lambda)$ with λ = 0, where (±) refers to the sectors with $C_{2z} = \pm i$. They can be expressed as

$$\begin{aligned}\nu^{(\pm)}(k_z) &= N_{\pm\frac{\pi}{4}}(k_z, \lambda = 0) + N_{\mp\frac{3\pi}{4}}(k_z, \lambda = 0)\\ &\equiv \mathcal{N}^{(\pm)}_{C_{4z}\mathcal{I}}(k_z)|_{\lambda=0} \mod 2,\end{aligned} \tag{25}$$

with $k_z = 0$ or π. Therefore, the differences between the total numbers of occupied states with $k_z = 0$ and that with $k_z = \pi$ are given by

$$\begin{aligned}\nu^{(\pm)}(\pi) - \nu^{(\pm)}(0) &\equiv \mathcal{N}^{(\pm)}_{C_{4z}\mathcal{I}}(\pi)|_{\lambda=0} - \mathcal{N}^{(\pm)}_{C_{4z}\mathcal{I}}(0)|_{\lambda=0}\\ &\equiv \chi^{(\pm)}_{C_{4z}\mathcal{I}} \mod 2.\end{aligned} \tag{26}$$

This equation means that the parity of the difference between $\nu^{\pm}(\pi)$ and $\nu^{\pm}(0)$ is determined by the numbers of occupied states with $C_{4z}\mathcal{I}$ eigenvalues at high-symmetry points. Therefore, when $\chi^{(+)}_{C_{4z}\mathcal{I}} \equiv 1 \bmod 2$, gapless states of $\mathcal{H}^{(+)}(k_z, \lambda = 0)$ appear, and the number of times the gapless states cross the

Fermi level between $k_z = 0$ and $k_z = \pi$ is odd. Similarly, when $\chi^{(-)}_{C_{4z}\mathcal{I}} \equiv 1 \bmod 2$, this holds in the $C_{2z} = -i$ sector.

Figure 5(c) shows an example when $\chi^{(+)}_{C_{4z}\mathcal{I}} \equiv \chi^{(-)}_{C_{4z}\mathcal{I}} \equiv 1 \bmod 2$. In Fig. 5(c), the numbers of occupied bands satisfy $\nu^{(\pm)}(0) = N^{(\pm)}_{\text{occ.}} - 1$ and $\nu^{(\pm)}(\pi) = N^{(\pm)}_{\text{occ.}}$, where $N^{(\pm)}_{\text{occ.}}$ is an integer. Therefore, the states in the $C_{2z} = +i$ sector cross the Fermi level an odd number of times and so do the states in the $C_{2z} = -i$ sector. As mentioned at the beginning of this section, we assume that the surfaces are gapped at $k_z = 0$ and $k_z = \pi$. Therefore, these states crossing the Fermi level are localized at the hinges in the real space, namely, these gapless states are hinge modes. Therefore, the hinge modes always appear in insulators with $C_{4z}\mathcal{I}$ symmetry when $\chi^{(+)}_{C_{4z}\mathcal{I}} \equiv \chi^{(-)}_{C_{4z}\mathcal{I}} \equiv 1 \bmod 2$.

Under the condition that the bulk and the surfaces are gapped at $k_z = 0$ and $k_z = \pi$, this scenario can be applied not only to insulators but also to WSMs [Fig. 5(d)]. In Fig. 5(d), the chiral hinge modes contribute to $\nu^{(\pm)}(\pi) - \nu^{(\pm)}(0)$, but the Fermi-arc surface states do not contribute to that. The model of the HOWSM in Sec. II corresponds to this case. On the other hand, another case of HOWSM is possible, where the Fermi-arc surface states account for the nonzero $\nu^{(\pm)}(\pi) - \nu^{(\pm)}(0)$, and the chiral hinge modes do not appear [Fig. 5(e)]. When $\chi^{(+)}_{C_{4z}\mathcal{I}} \equiv 1 \bmod 2$ and $\chi^{(-)}_{C_{4z}\mathcal{I}} \equiv 0 \bmod 2$, it leads to $\nu^{(+)}(\pi) - \nu^{(+)}(0) \equiv 1 \bmod 2$ and $\nu^{(-)}(\pi) - \nu^{(-)}(0) \equiv 0 \bmod 2$ [Fig. 5(f)]. The nonzero value of $\nu^{(+)}(\pi) - \nu^{(+)}(0)$ means that there should be gapless modes. Nonetheless, in this case, $\nu^{(+)}(\pi) - \nu^{(+)}(0)$ and $\nu^{(-)}(\pi) - \nu^{(-)}(0)$ are not equal. Therefore, these gapless modes are not hinge modes because a hinge mode at a given k_z ($\neq 0, \pi$) lying at two hinges related by C_{2z} symmetry leads to two modes, one with $C_{2z} = +i$ and the other with $C_{2z} = -i$. In this way, from Eq. (26), we can determine whether the gapless modes cross the Fermi level an odd number of times or an even number of times although whether the gapless modes are the hinge modes or the Fermi-arc surface states is not determined only by Eq. (26).

IV. CONCLUSION AND DISCUSSION

In summary, we show that when the topological invariants $\chi^{(\pm)}_{C_{4z}\mathcal{I}}$ are nontrivial, the chiral hinge modes appear, and thereby show general bulk-hinge correspondence for HOTPs. Our approach gives direct evidence to show the bulk-hinge correspondence only from the information of symmetry eigenvalues without relying on Dirac surface theory or on Wannier representations used in the previous works. In addition, we proposed a class of HOWSMs having the chiral hinge modes protected by rotoinversion $C_4\mathcal{I}$ symmetry in this paper. Unlike the HOWSMs in the previous works, which are characterized by topological invariants for the 2D HOTI and are realized by stacking the 2D HOTIs, the HOWSM in this paper has the chiral hinge modes characterized by the topological invariants for 3D HOTIs.

Finally, we discuss the possibilities of the material realizations of our HOWSMs with chiral hinge modes. Our model $\mathcal{H}_{\text{DSM}}(\boldsymbol{k})$ has similar energy spectra to a Dirac semimetal Cd_3As_2 [79–81] (see Appendix F). By adding perturbations to this model, we construct both the model of the HOWSMs protected by $C_4\mathcal{I}$ symmetry in Sec. II and the model protected by $\mathcal{I}$ symmetry in Appendix B. In addition, a recent experiment shows that Cd_3As_2 has hinge modes [31]. In terms of this experimental result and our theoretical results, we propose that our HOWSMs may be realized by adding perturbations such as magnetic doping or an external magnetic field to Cd_3As_2 [79,82] without breaking $C_4\mathcal{I}$ symmetry or $\mathcal{I}$ symmetry.

ACKNOWLEDGMENTS

This work was supported by JSPS KAKENHI Grants No. JP18H03678 and No. JP21J22264, and by JSPS Grant-in-Aid for Scientific Research on Innovative Areas “Discrete Geometric Analysis for Materials Design” Grants No. JP17H06469 and No. JP20H04633.

APPENDIX A: COMPARISON TO THE PREVIOUS WORKS

Here, we discuss the relationship between this work and the previous works. Although $C_{4z}\mathcal{I}$-symmetric bulk-hinge correspondence has been studied in previous works [7,73,74], they are merely indirect evidences to show that this bulk-hinge correspondence is reasonable. Discussions on the bulk-hinge correspondence with $C_{4z}\mathcal{I}$ symmetry in the previous works are classified into the following two types: (i) $\boldsymbol{k} \cdot \boldsymbol{p}$ surface theory [7] and (ii) the Wannier approach [74]. In approach (i), one starts from the surface Dirac Hamiltonian with a Dirac mass term, and shows that the Dirac mass term has a different sign between the two surfaces sharing the same hinge, resulting in the emergence of the chiral hinge modes. In approach (ii), one calculates the Wannier centers for two pseudo-2D systems corresponding to two subspaces at $k_z = 0$ and $k_z = \pi$. When excess corner charges obtained from the Wannier centers in the two subspaces are different, chiral hinge modes appear as a pumping of the corner charges. However, both of these approaches study only the special cases of $C_{4z}\mathcal{I}$-symmetric systems. Whether they hold in general remains unclear, except in cases that are adiabatically connected to those cases. Approach (i) cannot be applied to cases where the surface cannot be represented by a Dirac Hamiltonian. Approach (ii) is based on Wannier representations and assumes that electronic states are described in terms of localized Wannier functions. However, some electronic states, such as those with fragile topology [83], cannot be described in terms of localized Wannier states. On the other hand, our approach allows us to show emergence of the chiral hinge modes only from the $C_{4z}\mathcal{I}$-symmetry eigenvalues without relying on the Dirac surface Hamiltonian or on Wannier representations.

Next, we discuss the relationship between our topological invariants $\chi^{(\pm)}_{C_{4z}\mathcal{I}}$ and a topological invariant ν_c in Ref. [7]. In the previous work [7], the authors restrict themselves to systems with $\mathcal{IT}$ symmetry in order to define ν_c. Because $[\hat{C}_{4z}\hat{\mathcal{I}}, \hat{\mathcal{I}}\hat{\mathcal{T}}] = 0$ in $\mathcal{IT}$-symmetric systems and $\hat{\mathcal{I}}\hat{\mathcal{T}}$ is antiunitary, the eigenvalues of $C_{4z}\mathcal{I}$ at the high-symmetry points can be obtained by pairs $\{e^{i\frac{\pi}{4}}\xi_{n,\boldsymbol{k}}, e^{-i\frac{\pi}{4}}\xi_{n,\boldsymbol{k}}\}$, where $\xi_{n,\boldsymbol{k}} = \pm 1$, $n = 1, \ldots, N/2$, and N is the number of occupied bands. The topological invariant ν_c [7] is given by

$$(-1)^{\nu_c} = \prod_{n=1}^{N/2} \prod_{\boldsymbol{k} \in K_4} \xi_{n,\boldsymbol{k}}. \tag{A1}$$

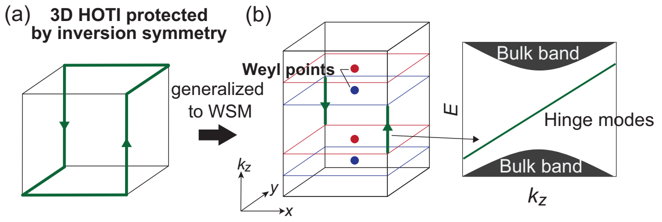

FIG. 6. (a) 3D HOTIs with the chiral hinge modes protected by $\mathcal{I}$ symmetry. (b) HOWSMs with the chiral hinge modes protected by $\mathcal{I}$ symmetry. They are characterized by the same topological invariants as that of the $\mathcal{I}$-symmetric HOTIs.

This topological invariant is well defined only in systems with both $C_{4z}\mathcal{I}$ symmetry and $\mathcal{IT}$ symmetry. On the other hand, our topological invariants $\chi^{(\pm)}_{C_{4z}\mathcal{I}}$ can be applied to general $C_{4z}\mathcal{I}$-symmetric systems.

In the following, we show that when a given system has $\mathcal{IT}$ symmetry, the topologically nontrivial case in our theory, $\chi^{(+)}_{C_{4z}\mathcal{I}} \equiv \chi^{(-)}_{C_{4z}\mathcal{I}} \equiv 1 \mod 2$ is equivalent to the case with $\nu_c \equiv 1 \mod 2$. The topological invariant ν_c can be rewritten as

$$\nu_c \equiv \frac{1}{2}\sum_{\boldsymbol{k}\in K_4} n_{\xi_{\boldsymbol{k}},-}(\boldsymbol{k}) \mod 2, \tag{A2}$$

where $n_{\xi_{\boldsymbol{k}},-}(\boldsymbol{k})$ is the number of occupied states with $\xi_{n,\boldsymbol{k}} = -1$, and $n_{\xi_{\boldsymbol{k}},-}(\boldsymbol{k})$ is an even number because the eigenvalues of $C_{4z}\mathcal{I}$ at $\boldsymbol{k} \in K_4$ are given by a pair $\{e^{i\frac{\pi}{4}}\xi_{n,\boldsymbol{k}}, e^{-i\frac{\pi}{4}}\xi_{n,\boldsymbol{k}}\}$. Now that we are considering an insulator, our topological invariants $\chi^{(\pm)}_{C_{4z}\mathcal{I}}$ are given by Eqs. (11) and (12). In addition, the pair $\{e^{i\frac{\pi}{4}}\xi_{n,\boldsymbol{k}}, e^{-i\frac{\pi}{4}}\xi_{n,\boldsymbol{k}}\}$ leads to $n_{+\frac{\pi}{4}}(\boldsymbol{k}) = n_{-\frac{\pi}{4}}(\boldsymbol{k})$, and therefore we obtain

$$\begin{aligned}\nu_c &\equiv \frac{1}{2}\sum_{\boldsymbol{k}\in K_4}\left(n_{+\frac{3\pi}{4}}(\boldsymbol{k}) + n_{-\frac{3\pi}{4}}(\boldsymbol{k})\right)\\ &= \frac{1}{2}\sum_{\boldsymbol{k}\in K_4}\left(\nu - n_{+\frac{\pi}{4}}(\boldsymbol{k}) - n_{-\frac{\pi}{4}}(\boldsymbol{k})\right)\\ &= \frac{1}{2}\sum_{\boldsymbol{k}\in K_4}\left(\nu - 2n_{+\frac{\pi}{4}}(\boldsymbol{k})\right)\\ &\equiv \chi^{(+)}_{C_{4z}\mathcal{I}} \mod 2,\end{aligned} \tag{A3}$$

where ν is the number of occupied bands in the bulk. Furthermore, by using $n_{+\frac{\pi}{4}}(\boldsymbol{k}) = n_{-\frac{\pi}{4}}(\boldsymbol{k})$, we get

$$\chi^{(+)}_{C_{4z}\mathcal{I}} \equiv \chi^{(-)}_{C_{4z}\mathcal{I}} \mod 2. \tag{A4}$$

By combining Eqs. (A3) and (A4), we find that $\chi^{(+)}_{C_{4z}\mathcal{I}} \equiv \chi^{(-)}_{C_{4z}\mathcal{I}} \equiv 1 \mod 2$ is equivalent to $\nu_c \equiv 1 \mod 2$.

APPENDIX B: HIGHER-ORDER WEYL SEMIMETALS PROTECTED BY INVERSION SYMMETRY

In the main text, we discussed a HOWSM protected by $C_{4z}\mathcal{I}$ symmetry. For comparison, in this Appendix, we discuss a HOWSM with chiral hinge modes protected by $\mathcal{I}$ symmetry in class A, one of the Altland-Zirnbauer symmetry classes [84]. This HOWSM is regarded as a generalization of the 3D HOTIs protected by $\mathcal{I}$ symmetry [Figs. 6(a) and 6(b)].

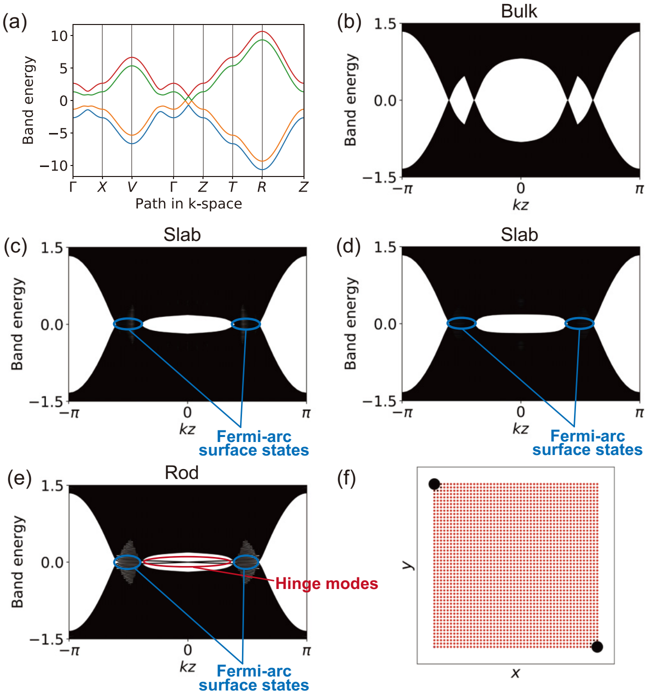

FIG. 7. HOWSM with chiral hinge modes protected by $\mathcal{I}$ symmetry. (a) Bulk band structure of the tight-binding model of Eq. (B2) along the high-symmetry lines. (b) The band structure with the periodic boundary conditions in the x and y directions and with various values of k_x and k_y. (c) The band structure with the open boundary condition in the x direction and the periodic boundary condition in the y direction and with various values of k_y, where the system size is $L_x = 200$ in the x direction. (d) The band structure with the open boundary condition in the y direction and the periodic boundary condition in the x direction and with various values of k_x, where the system size is $L_y = 200$ in the y direction. (e) The band structure with the open boundary conditions in the x and the y directions, where the system size is $L_x \times L_y = 50 \times 50$. (f) The real-space distribution of zero-energy modes of (e).

Similarly to the HOWSM protected by $C_{4z}\mathcal{I}$ symmetry in Sec. II, we start from Eq. (3) of the Hamiltonian for a 3D Dirac semimetal. This model is defined on a primitive orthorhombic lattice. In the following, we set the lattice constants to 1. We add perturbations

$$\mathcal{H}_{\mathcal{I}} = \left(\sum_{j=x,y,z} B_j\sigma_j\right)\tau_0 + v_f \sin k_z\sigma_x\tau_y \tag{B1}$$

to this Dirac semimetal. These perturbations preserve $\mathcal{I}$ symmetry, and the overall Hamiltonian can be expressed as

$$\mathcal{H}'(\boldsymbol{k}) = \mathcal{H}_{\mathrm{DSM}}(\boldsymbol{k}) + \mathcal{H}_{\mathcal{I}}. \tag{B2}$$

In the following, we set the parameters of the model $\mathcal{H}'(\boldsymbol{k})$ as $m = 4$, $c = 2$, $v = 1$, $v_f = 0.05$, $B_x = B_y = 0.3$, and $B_z = 0.5$, and we set the Fermi level to be zero. The high-symmetry points in the Brillouin zone are given by $\Gamma = (0, 0, 0)$, $X = (\pi, 0, 0)$, $V = (\pi, \pi, 0)$, $Z = (0, 0, \pi)$, $T = (0, \pi, \pi)$, and $R = (\pi, \pi, \pi)$. Figure 7(a) shows band structures of the bulk Hamiltonian $\mathcal{H}'(\boldsymbol{k})$ along the high-symmetry lines.

This model has $\mathcal{I}$ symmetry,

$$\mathcal{I}\mathcal{H}'(\boldsymbol{k})\mathcal{I}^{-1} = \mathcal{H}'(-\boldsymbol{k}), \tag{B3}$$

and therefore the parity eigenvalues of occupied states are well defined at the $\mathcal{I}$-symmetric momenta in the k-space. These $\mathcal{I}$-symmetric momenta can be written as $\Gamma_{j=(n_x,n_y,n_z)} = (n_x\boldsymbol{b}_x + n_y\boldsymbol{b}_y + n_z\boldsymbol{b}_z)/2$ with three integers $n_l = 0, 1$ defined modulo 2, where $\boldsymbol{b}_l$ represents primitive reciprocal lattice vectors. Here we consider the space group No. 2 ($P\bar{1}$) generated by $\mathcal{I}$. Because we do not assume $\mathcal{T}$ symmetry, it is the type-I magnetic space group No. 2.4 generated by $\mathcal{I}$. Its symmetry-based indicators are given by $X_{\mathrm{BS}} = \mathbb{Z}_2 \times \mathbb{Z}_2 \times \mathbb{Z}_2 \times \mathbb{Z}_4$ [63]. The three $\mathbb{Z}_2$ factors are weak topological indices and can be written as

$$\nu_a \equiv \sum_{\Gamma_j \wedge n_a = 1} n_-(\Gamma_j) \mod 2 \quad (a = x, y, z), \tag{B4}$$

where $n_-(\Gamma_i)$ denotes the numbers of odd-parity occupied states at Γ_j, and the summation is taken over the $\mathcal{I}$-symmetric momenta on the plane $n_a = 1$. These weak indices ν_x, ν_y, and ν_z correspond to Chern numbers on the $k_x = 0$, $k_y = 0$, and $k_z = 0$ planes, respectively. When these indices are nontrivial, the gapless surface states appear and mask possible hinge modes. Therefore, we assume these indices are trivial. On the other hand, the $\mathbb{Z}_4$ index of X_{BS} is given by an integer μ_1 [65] written as

$$\mu_1 \equiv \frac{1}{2}\sum_{\Gamma_j}(n_+(\Gamma_j) - n_-(\Gamma_j)) \mod 4, \tag{B5}$$

where $n_+(\Gamma_j)$ is the number of even-parity occupied states at the $\mathcal{I}$-symmetric momenta Γ_j. In the previous work [71], the authors showed that when $\mu_1 = 2$ and $\nu_a = 0$ $(a = x, y, z)$, hinge modes always appear in systems with $\mathcal{I}$ symmetry. Although this bulk-hinge correspondence for HOTPs focuses on insulators, this theory can be also applied to WSMs when Fermi-arc surface states do not cover the hinge modes. The parity eigenvalues of occupied states at the $\mathcal{I}$-symmetric momenta in our model satisfy $\nu_x = \nu_y = \nu_z = 0$ and $\mu_1 = 2$.

To see behaviors of the hinge modes and the surface states of our model, we calculate band structures in the bulk, in the slab, and in the rod geometries, and compare them. Figures 7(b)–7(e) show the band structures with these different geometries. These model calculations were performed using the PYTHTB package [76]. The system has surfaces in both Fig. 7(c) and Fig. 7(d), and the Fermi-arc surface states appear in these cases. In Fig. 7(e), the system has surfaces and hinges, resulting in the emergence of the hinge modes. The zero-energy modes are localized at the corners in the real space [Fig. 7(f)], and here the surface states have a minigap because of the finite-size effects. The hinge modes are localized at the two corners facing in opposite directions in the real space, unlike the $C_{4z}\mathcal{I}$-symmetric HOWSM where the hinge modes appear at four corners in Sec. II.

APPENDIX C: CLASSIFICATION OF TOPOLOGICAL PHASES BASED ON SYMMETRY-BASED INDICATORS

In this Appendix, we review the classifications of topological phases in type-I magnetic space groups based on Ref. [65] to see which magnetic space groups allow HOTPs with chiral hinge modes. According to Ref. [65], it is sufficient to discuss the following seven key space groups, $P\bar{1}$, Pn, Pn/m, $P\bar{4}$, $Pmmm$ (spinful), $P4/mmm$ (spinful), and $Pcc2$ (spinless), where the strong indices of the symmetry-based indicators are given by μ_1 ($P\bar{1}$), a mirror Chern number (Pn/m), Chern number ($P\bar{4}$), μ_4 ($P\bar{4}$), κ_1 ($Pmmm$), $\Delta = \kappa_1 - 2\kappa_4$ ($P4/mmm$), and μ_2 ($Pcc2$). κ_1 is the indicator to detect HOTPs with helical hinge modes. A mirror Chern number and Δ are the indicators to detect topological crystalline insulator phases protected by mirror symmetries leading to gapless surface states on mirror-invariant surfaces. Similarly, μ_2 is the indicator for a topological crystalline insulator protected by glide symmetries leading to gapless surface states on glide-invariant surfaces. Thus, only μ_1 and μ_4 can capture HOTPs with chiral hinge modes, and therefore the chiral hinge modes are limited to ones protected by $\mathcal{I}$ symmetry and ones protected by $C_4\mathcal{I}$ symmetry.

APPENDIX D: SYMMETRY-BASED INDICATORS AND THE DIFFERENCE BETWEEN THE CHERN NUMBERS ON THE $k_z = 0$ AND $k_z = \pi$ PLANES

In this Appendix, we show Eq. (13) in Sec. II. Here we consider a general spinful 3D insulator with $C_{4z}\mathcal{I}$ symmetry, and the high-symmetry points in the k-space are given by $\Gamma = (0, 0, 0)$, $M = (\pi, \pi, 0)$, $Z = (0, 0, \pi)$, $A = (\pi, \pi, \pi)$, $X = (0, \pi, 0)$, and $R = (0, \pi, \pi)$ [see Fig. 2(c)]. On the $k_z = 0$ and $k_z = \pi$ planes, the $C_{4z}\mathcal{I}$ operation changes the wave vectors as $(k_x, k_y, k_z) \to (k_y, -k_x, k_z)$. Similar to the formula of the Chern number expressed in terms of rotation eigenvalues in Ref. [85], we can easily derive the formula of the Chern number in terms of the $C_{4z}\mathcal{I}$- and C_{2z}-symmetry eigenvalues as

$$i^{\mathrm{Ch}|_{k_z=0}} = \prod_{n:\mathrm{occ.}} -\xi_n(\Gamma)\xi_n(M)\zeta_n(Y), \tag{D1}$$

$$i^{\mathrm{Ch}|_{k_z=\pi}} = \prod_{n:\mathrm{occ.}} -\xi_n(Z)\xi_n(A)\zeta_n(R), \tag{D2}$$

where $\xi_n(\boldsymbol{k})$ and $\zeta_n(\boldsymbol{k})$ are eigenvalues of $C_{4z}\mathcal{I}$ and C_{2z} at $C_{4z}\mathcal{I}$-invariant momenta $\boldsymbol{k}$, respectively. Here, the following equations hold:

$$\prod_{n:\mathrm{occ.}} \xi_n(\boldsymbol{k}) = \prod_{\alpha} \exp[i\alpha n_\alpha(\boldsymbol{k})], \tag{D3}$$

$$\prod_{n:\mathrm{occ.}} \zeta_n(\boldsymbol{k}) = \prod_{\beta} \exp\left[i\beta n^{(\beta)}_{C_{2z}}(\boldsymbol{k})\right], \tag{D4}$$

where α runs over $\alpha = \pm\pi/4, \pm3\pi/4$, and β runs over $\beta = \pm\pi/2$, and $n_\alpha(\boldsymbol{k})$ denotes the numbers of occupied states with the $C_{4z}\mathcal{I}$ eigenvalues $e^{i\alpha}$. Similarly, $n^{(\beta)}_{C_{2z}}(\boldsymbol{k})$ is the number of occupied states with the C_{2z} eigenvalues $e^{i\beta}$. By combining Eqs. (D1) and (D2), we obtain the following equation:

$$\begin{aligned} i^{(\mathrm{Ch}|_{k_z=\pi} - \mathrm{Ch}|_{k_z=0})} &= \prod_{\alpha} \exp[i\alpha(n_\alpha(Z) + n_\alpha(A) - n_\alpha(\Gamma) - n_\alpha(M))] \\ &\quad \times \prod_{\beta} \exp[i\beta(n^{(\beta)}_{C_{2z}}(R) - n^{(\beta)}_{C_{2z}}(X))]. \end{aligned} \tag{D5}$$

By using a compatibility relation of C_{2z} symmetry along the high-symmetry line X-R,

$$n^{(\beta)}_{C_{2z}}(X) = n^{(\beta)}_{C_{2z}}(R), \tag{D6}$$

we rewrite Eq. (D5) as

$$\begin{aligned}
i^{(\mathrm{Ch}|_{k_z=\pi}-\mathrm{Ch}|_{k_z=0})} &= \prod_{\alpha} \exp[i\alpha(n_\alpha(Z)+n_\alpha(A)-n_\alpha(\Gamma)-n_\alpha(M))] \\
&= \exp\Bigg[i\frac{\pi}{4} \sum_{\boldsymbol{k}\in Z,A} \big(n_{+\frac{\pi}{4}}(\boldsymbol{k}) + 3n_{+\frac{3\pi}{4}}(\boldsymbol{k}) - n_{-\frac{\pi}{4}}(\boldsymbol{k}) - 3n_{-\frac{3\pi}{4}}(\boldsymbol{k})\big) \\
&\quad - i\frac{\pi}{4} \sum_{\boldsymbol{k}\in \Gamma,M} \big(n_{+\frac{\pi}{4}}(\boldsymbol{k}) + 3n_{+\frac{3\pi}{4}}(\boldsymbol{k}) - n_{-\frac{\pi}{4}}(\boldsymbol{k}) - 3n_{-\frac{3\pi}{4}}(\boldsymbol{k})\big)\Bigg] \\
&= \exp\Bigg[i\frac{\pi}{4} \sum_{\boldsymbol{k}\in Z,A} \big(n_{+\frac{\pi}{4}}(\boldsymbol{k}) + n_{-\frac{3\pi}{4}}(\boldsymbol{k}) - n_{+\frac{3\pi}{4}}(\boldsymbol{k}) - n_{-\frac{\pi}{4}}(\boldsymbol{k})\big) \\
&\quad - i\frac{\pi}{4} \sum_{\boldsymbol{k}\in \Gamma,M} \big(n_{+\frac{\pi}{4}}(\boldsymbol{k}) + n_{-\frac{3\pi}{4}}(\boldsymbol{k}) - n_{+\frac{3\pi}{4}}(\boldsymbol{k}) - n_{-\frac{\pi}{4}}(\boldsymbol{k})\big)\Bigg] \\
&\quad \times \exp\Bigg[i\pi \sum_{\boldsymbol{k}\in Z,A} \big(n_{+\frac{3\pi}{4}}(\boldsymbol{k}) - n_{-\frac{3\pi}{4}}(\boldsymbol{k})\big) - i\pi \sum_{\boldsymbol{k}\in \Gamma,M} \big(n_{+\frac{3\pi}{4}}(\boldsymbol{k}) - n_{-\frac{3\pi}{4}}(\boldsymbol{k})\big)\Bigg] \\
&= \exp\Bigg[i\pi \sum_{\boldsymbol{k}\in Z,A} \big(n_{+\frac{3\pi}{4}}(\boldsymbol{k}) - n_{-\frac{3\pi}{4}}(\boldsymbol{k})\big) - i\pi \sum_{\boldsymbol{k}\in \Gamma,M} \big(n_{+\frac{3\pi}{4}}(\boldsymbol{k}) - n_{-\frac{3\pi}{4}}(\boldsymbol{k})\big)\Bigg],
\end{aligned} \tag{D7}$$

where the last equality follows from the compatibility relations of the C_{2z}-symmetry eigenvalues along the high-symmetry lines Γ-Z and M-A:

$$\begin{aligned}
n_{+\frac{\pi}{4}}(\Gamma) + n_{-\frac{3\pi}{4}}(\Gamma) &= n_{+\frac{\pi}{4}}(Z) + n_{-\frac{3\pi}{4}}(Z), \\
n_{-\frac{\pi}{4}}(\Gamma) + n_{+\frac{3\pi}{4}}(\Gamma) &= n_{-\frac{\pi}{4}}(Z) + n_{+\frac{3\pi}{4}}(Z), \\
n_{+\frac{\pi}{4}}(M) + n_{-\frac{3\pi}{4}}(M) &= n_{+\frac{\pi}{4}}(A) + n_{-\frac{3\pi}{4}}(A), \\
n_{-\frac{\pi}{4}}(M) + n_{+\frac{3\pi}{4}}(M) &= n_{-\frac{\pi}{4}}(A) + n_{+\frac{3\pi}{4}}(A).
\end{aligned}$$

Noting that $\exp[-i2\pi(n_{+\frac{3\pi}{4}}(\boldsymbol{k}) - n_{-\frac{3\pi}{4}}(\boldsymbol{k}))] = 1$, we obtain the following equation:

$$i^{(\mathrm{Ch}|_{k_z=\pi}-\mathrm{Ch}|_{k_z=0})} = \exp[i\pi\Delta'], \tag{D8}$$

with

$$\Delta' \equiv \sum_{\boldsymbol{k}\in K_4} \big(n_{+\frac{3\pi}{4}}(\boldsymbol{k}) - n_{-\frac{3\pi}{4}}(\boldsymbol{k})\big) \bmod 2, \tag{D9}$$

where K_4 are the $C_{4z}\mathcal{I}$-symmetric momenta $K_4 = \{\Gamma, M, Z, A\}$. Furthermore, Δ' can be expressed as

$$\begin{aligned}
\Delta' &\equiv \sum_{\boldsymbol{k}\in K_4} \big(\nu - n_{+\frac{\pi}{4}}(\boldsymbol{k}) - n_{-\frac{\pi}{4}}(\boldsymbol{k})\big) \\
&\equiv \sum_{\boldsymbol{k}\in K_4} \big(n_{+\frac{\pi}{4}}(\boldsymbol{k}) + n_{-\frac{\pi}{4}}(\boldsymbol{k})\big) \bmod 2,
\end{aligned} \tag{D10}$$

where ν is a number of occupied bands in the bulk. Therefore, by using the topological indices $\chi^{(+)}_{C_4\mathcal{I}}$ and $\chi^{(+)}_{C_4\mathcal{I}}$ [see Eq. (11), and Eq. (12) in Sec. II], we can rewrite Δ' as

$$\Delta' \equiv \chi^{(+)}_{C_4\mathcal{I}} + \chi^{(-)}_{C_4\mathcal{I}} \bmod 2. \tag{D11}$$

By combining Eqs. (D8) and (D11), we get Eq. (13).

APPENDIX E: PROPERTIES OF SPECTRAL FLOWS WITH ROTOINVERSION EIGENVALUES

In this Appendix, we show the following three properties of the spectral flows in the cutting procedures that we use in Sec. III B:

(i) When the cutting parameter is $\lambda = -1$, the wave vectors in the x and y directions are $k_i = \frac{2\pi}{L_i}m_i + \frac{\pi}{L_i}$ $(-M \leqslant m_i \leqslant M)$ $(i = x, y)$.

(ii) The spectral flows in the band gap are symmetric under $\lambda \leftrightarrow -\lambda$, namely, $E(k_z, \lambda) = E(k_z, -\lambda)$.

(iii) When a state with the energy $E(k_z, \lambda)$ has the $e^{i\alpha}$ eigenvalue, a state with the energy $E(k_z, -\lambda)$ has the $-e^{i\alpha}$ eigenvalue ($\alpha = \pi/4$, $-\pi/4$, $3\pi/4$, and $-3\pi/4$).

We assume M to be sufficiently large.

The Hamiltonian considered in Sec. III B can be expressed as

$$\begin{aligned}
\mathcal{H}(k_z, \lambda) = &\sum_{x=-M}^{M} \sum_{y=-M}^{M} H_0(k_z) \otimes |x, y\rangle\langle x, y| \\
&+ \sum_{x=-M}^{M-1} \sum_{y=-M}^{M} [H_x(k_z) \otimes |x+1, y\rangle\langle x, y| + \mathrm{H.c.}] \\
&+ \sum_{y=-M}^{M} [\lambda H_x(k_z) \otimes |-M, y\rangle\langle M, y| + \mathrm{H.c.}] \\
&+ \sum_{x=-M}^{M} \sum_{y=-M}^{M-1} [H_y(k_z) \otimes |x, y+1\rangle\langle x, y| + \mathrm{H.c.}] \\
&+ \sum_{x=-M}^{M} [\lambda H_y(k_z) \otimes |x, -M\rangle\langle x, M| + \mathrm{H.c.}],
\end{aligned} \tag{E1}$$

where $H_0(k_z)$, $H_x(k_z)$, and $H_y(k_z)$ are $n \times n$ matrices, with n being the number of internal degrees of freedom per site. For simplicity, we consider a case where the hopping is limited up to the nearest-neighbor unit cells. The following discussions can be easily extended to the case with mth-nearest-neighbor hoppings as long as $m \ll M$.

1. Proof of $k_i = (2m_i + 1)\pi/L_i$ when $\lambda = -1$

Here, we show that by changing the cutting parameter from $\lambda = 1$ to $\lambda = -1$, the wave vectors are shifted as $k_i = 2m_i\pi/L_i \to (2m_i + 1)\pi/L_i$. In fact, this is obvious from the fact that $\lambda = 1$ and $\lambda = -1$ correspond to periodic and antiperiodic boundary conditions, respectively. Here, we show this explicitly for the purpose of using the results to prove other properties in the following sections. Here, the translation operators T_x and T_y are defined as

$$\begin{aligned}
T_x &\equiv \sum_{x=-M}^{M-1}\sum_{y=-M}^{M}[|x+1,y\rangle\langle x,y|] + \sum_{y=-M}^{M}[|-M,y\rangle\langle M,y|],\\
T_y &\equiv \sum_{x=-M}^{M}\sum_{y=-M}^{M-1}[|x,y+1\rangle\langle x,y|] + \sum_{x=-M}^{M}[|x,-M\rangle\langle x,M|].
\end{aligned}\tag{E2}$$

Therefore, when $\lambda = 1$, the Hamiltonian can be expressed as

$$\begin{aligned}
\mathcal{H}(k_z,\lambda=1) = &\sum_{x=-M}^{M}\sum_{y=-M}^{M} H_0(k_z)\otimes|x,y\rangle\langle x,y|\\
&+ [H_x\otimes T_x + H_y\otimes T_y + \text{H.c.}].
\end{aligned}\tag{E3}$$

In addition, we introduce two unitary transformations

$$U_x = \exp\left(i\frac{\pi}{L_x}\hat{x}\right),\ U_y = \exp\left(i\frac{\pi}{L_y}\hat{y}\right).\tag{E4}$$

By using these unitary transformations, we can obtain the following equation:

$$\begin{aligned}
&U_xU_y\mathcal{H}(k_z,\lambda)(U_xU_y)^{-1}\\
&= \sum_{x=-M}^{M}\sum_{y=-M}^{M} H_0(k_z)\otimes|x,y\rangle\langle x,y|\\
&+ \sum_{x=-M}^{M-1}\sum_{y=-M}^{M}\left[e^{i\frac{\pi}{L_x}}H_x\otimes|x+1,y\rangle\langle x,y| + \text{H.c.}\right]\\
&+ \sum_{y=-M}^{M}\left[-\lambda e^{i\frac{\pi}{L_x}}H_x\otimes|-M,y\rangle\langle M,y| + \text{H.c.}\right]\\
&+ \sum_{x=-M}^{M}\sum_{y=-M}^{M-1}\left[e^{i\frac{\pi}{L_y}}H_y\otimes|x,y+1\rangle\langle x,y| + \text{H.c.}\right]\\
&+ \sum_{x=-M}^{M}\left[-\lambda e^{i\frac{\pi}{L_x}}H_y\otimes|x,-M\rangle\langle x,M| + \text{H.c.}\right].
\end{aligned}\tag{E5}$$

When $\lambda = -1$, this equation can be expressed as

$$\begin{aligned}
&U_xU_y\mathcal{H}(k_z,\lambda=-1)(U_xU_y)^{-1}\\
&\quad= \sum_{x=-M}^{M}\sum_{y=-M}^{M} H_0(k_z)\otimes|x,y\rangle\langle x,y|\\
&\qquad+ [H_x\otimes\tilde{T}_x + H_y\otimes\tilde{T}_y + \text{H.c.}],
\end{aligned}\tag{E6}$$

where $\tilde{T}_x \equiv e^{i\frac{\pi}{L_x}}T_x$ and $\tilde{T}_y \equiv e^{i\frac{\pi}{L_y}}T_y$. The eigenvalues of T_i and $\tilde{T}_i$ $(i = x, y)$ are defined by e^{ik_i} and $e^{i\tilde{k}_i}$, respectively, and these wave vectors are given by

$$k_i = \frac{2\pi}{L_i}m_i\ \ (-M \leqslant m_i \leqslant M),\tag{E7}$$

$$\tilde{k}_i = \frac{2\pi}{L_i}m_i + \frac{\pi}{L_i}\ \ (-M \leqslant m_i \leqslant M),\tag{E8}$$

with $i = x, y$. From this, we conclude that $U_xU_y\mathcal{H}(k_z,\lambda = -1)(U_xU_y)^{-1}$ is unitary equivalent to $\mathcal{H}(k_z,\lambda = 1)$ with the wave vector being shifted as $k_i \to k_i + \frac{\pi}{L_i}$. In other words, by changing λ from -1 to 1, the wave vectors are shifted as $k_i = 2m_i\pi/L_i \to (2m_i + 1)\pi/L_i$.

2. Proof of $E(k_z, \lambda) = E(k_z, -\lambda)$ for spectral flows

Here, we show that the spectral flows in the band gap are symmetric under $\lambda \leftrightarrow -\lambda$ when L_x $(= L_y)$ is sufficiently large. By approximating $e^{i\frac{\pi}{L_x}} \approx 1$ and $e^{i\frac{\pi}{L_y}} \approx 1$, from Eq. (E5), we obtain the following equation:

$$U_xU_y\mathcal{H}(k_z,\lambda)(U_xU_y)^{-1} \approx \mathcal{H}(k_z,-\lambda),\tag{E9}$$

where L_x and L_y are sufficiently large. Therefore, under the unitary transformations U_x and U_y, $\mathcal{H}(k_z,\lambda)$ can be transformed into $\mathcal{H}(k_z,-\lambda)$, and these two Hamiltonians have the same energy: $E(k_z,\lambda) = E(k_z,-\lambda)$. In other words, the spectral flows are symmetric under $\lambda \leftrightarrow -\lambda$ when L_x and L_y are sufficiently large.

3. Spectral flows with the opposite rotoinversion eigenvalues

Next, we give a proof that when a state with the energy $E(k_z,\lambda)$ has an $e^{i\alpha}$ eigenvalue of $C_{4z}\mathcal{I}$ $(\alpha = \pm\pi/4, \pm3\pi/4)$, a state with the energy $E(k_z,-\lambda)$ has the $-e^{i\alpha}$ eigenvalue. In the previous section, we showed that $U_xU_y\mathcal{H}(k_z,\lambda)(U_xU_y)^{-1} \approx \mathcal{H}(k_z,-\lambda)$ when L_x and L_y are sufficiently large. Therefore, the following equation holds:

$$\mathcal{H}(k_z,-\lambda)U_xU_y|\psi_\alpha(k_z,\lambda)\rangle = EU_xU_y|\psi_\alpha(k_z,\lambda)\rangle,\tag{E10}$$

when $\mathcal{H}(k_z,\lambda)$ has an eigenstate $|\psi_\alpha(k_z,\lambda)\rangle$ with the $e^{i\alpha}$ eigenvalue $(\alpha = \pm\pi/4, \pm3\pi/4)$ of $C_{4z}\mathcal{I}$. From this, we obtain the following equation:

$$\begin{aligned}
C_{4z}\mathcal{I}U_xU_y|\psi_\alpha(k_z,\lambda)\rangle &= U_yU_x^\dagger C_{4z}\mathcal{I}|\psi_\alpha(k_z,\lambda)\rangle\\
&= (U_x^\dagger)^2U_xU_ye^{i\alpha}|\psi_\alpha(k_z,\lambda)\rangle\\
&= e^{i\frac{2\pi}{L_x}\hat{x}}U_xU_ye^{i\alpha}|\psi_\alpha(k_z,\lambda)\rangle\\
&\simeq -e^{i\alpha}U_xU_y|\psi_\alpha(k_z,\lambda)\rangle,
\end{aligned}\tag{E11}$$

where $x \simeq \pm M$. Therefore, the localized states $|\psi_\alpha(k_z,\lambda)\rangle$ and $U_xU_y|\psi_\alpha(k_z,\lambda)\rangle$ at the boundary $x \simeq \pm M$ have opposite eigenvalues, $e^{i\alpha}$ and $-e^{i\alpha}$, respectively.

APPENDIX F: RELATIONSHIP BETWEEN $\mathcal{H}_{\mathrm{DSM}}(\vec{k})$ AND AN EFFECTIVE HAMILTONIAN FOR $\mathrm{Cd_3As_2}$

In this Appendix, we show that our model $\mathcal{H}_{\mathrm{DSM}}(\boldsymbol{k})$ for a Dirac semimetal [Eq. (3)] has similar energy spectra to an effective $\boldsymbol{k}\cdot\boldsymbol{p}$ model for $\mathrm{Cd_3As_2}$ known as a Dirac semimetal [79–81]. $\mathrm{Cd_3As_2}$ respects space groups No. 137 ($P4_2/nmc1'$) and No. 142 ($I4_1/acd1'$) at room temperature and high temperature, respectively [79,81]. When $\mathrm{Cd_3As_2}$ has such centrosymmetric structures, the effective Hamiltonian [79] around the Γ point is given by

$$\mathcal{H}_\Gamma(\boldsymbol{k}) = \epsilon_0(\boldsymbol{k}) + \begin{pmatrix} M(\boldsymbol{k}) & Ak_+ & 0 & 0 \\ Ak_- & -M(\boldsymbol{k}) & 0 & 0 \\ 0 & 0 & M(\boldsymbol{k}) & -Ak_- \\ 0 & 0 & -Ak_+ & -M(\boldsymbol{k}) \end{pmatrix} + O(k^2), \tag{F1}$$

in terms of the four bases $|S_{J=\frac{1}{2}}, J_z=\frac{1}{2}\rangle$, $|P_{J=\frac{3}{2}}, J_z=\frac{3}{2}\rangle$, $|S_{J=\frac{1}{2}}, J_z=-\frac{1}{2}\rangle$, and $|P_{J=\frac{3}{2}}, J_z=-\frac{3}{2}\rangle$, where $\epsilon_0(\boldsymbol{k}) = C_0 + C_1k_z^2 + C_2(k_x^2+k_y^2)$, $k_\pm = k_x \pm ik_y$, and $M(\boldsymbol{k}) = M_0 - M_1k_z^2 - M_2(k_x^2+k_y^2)$ with parameters $M_0 < 0$, $M_1 < 0$, and $M_2 < 0$. We can rewrite this Hamiltonian as

$$\mathcal{H}_\Gamma(\boldsymbol{k}) = \epsilon_0(\boldsymbol{k}) + A(k_x\sigma_z\tau_x - k_y\sigma_0\tau_y) + M(\boldsymbol{k})\sigma_0\tau_z + O(k^2), \tag{F2}$$

where σ_i and τ_i ($i = x, y, z$) are the Pauli matrices corresponding to $J_z = \pm J$ and $J = \frac{3}{2}, \frac{1}{2}$, respectively. By using a unitary matrix

$$U_D = \sigma_x\frac{\tau_x - i\tau_y}{2} + \sigma_z\frac{\tau_x + i\tau_y}{2}, \tag{F3}$$

we can obtain the following equation:

$$\begin{aligned}\mathcal{H}'_\Gamma(\boldsymbol{k}) &\equiv U_D\mathcal{H}_\Gamma(\boldsymbol{k})U_D^\dagger \\ &= \epsilon_0(\boldsymbol{k}) + A(k_x\sigma_x\tau_x + k_y\sigma_y\tau_x) - M(\boldsymbol{k})\sigma_0\tau_z + O(k^2).\end{aligned} \tag{F4}$$

The energy dispersion of $\mathcal{H}'_\Gamma(\boldsymbol{k})$ is given by $E(\boldsymbol{k}) = \epsilon_0(\boldsymbol{k}) \pm \sqrt{M(\boldsymbol{k}) + A^2k_+k_-}$, resulting in a pair of Dirac points at $(k_x, k_y, k_z) = (0, 0, \pm\sqrt{\frac{M_0}{M_1}})$. If we set $\epsilon_0(\boldsymbol{k})$ to be zero, $\mathcal{H}'_\Gamma(\boldsymbol{k})$ is identical to the expansion of $\mathcal{H}_{\mathrm{DSM}}(\boldsymbol{k})$ [Eq. (3)] to the second order k^2 around the Γ point.

---

[1] M. Sitte, A. Rosch, E. Altman, and L. Fritz, Topological Insulators in Magnetic Fields: Quantum Hall Effect and Edge Channels with a Nonquantized θ Term, Phys. Rev. Lett. **108**, 126807 (2012).

[2] F. Zhang, C. L. Kane, and E. J. Mele, Surface State Magnetization and Chiral Edge States on Topological Insulators, Phys. Rev. Lett. **110**, 046404 (2013).

[3] W. A. Benalcazar, B. A. Bernevig, and T. L. Hughes, Quantized electric multipole insulators, Science **357**, 61 (2017).

[4] W. A. Benalcazar, B. A. Bernevig, and T. L. Hughes, Electric multipole moments, topological multipole moment pumping, and chiral hinge states in crystalline insulators, Phys. Rev. B **96**, 245115 (2017).

[5] Z. Song, Z. Fang, and C. Fang, $(d-2)$-Dimensional Edge States of Rotation Symmetry Protected Topological States, Phys. Rev. Lett. **119**, 246402 (2017).

[6] J. Langbehn, Y. Peng, L. Trifunovic, F. von Oppen, and P. W. Brouwer, Reflection-Symmetric Second-Order Topological Insulators and Superconductors, Phys. Rev. Lett. **119**, 246401 (2017).

[7] F. Schindler, A. M. Cook, M. G. Vergniory, Z. Wang, S. S. Parkin, B. A. Bernevig, and T. Neupert, Higher-order topological insulators, Sci. Adv. **4**, eaat0346 (2018).

[8] C. Fang and L. Fu, New classes of topological crystalline insulators having surface rotation anomaly, Sci. Adv. **5**, eaat2374 (2019).

[9] M. Z. Hasan and C. L. Kane, Colloquium: Topological insulators, Rev. Mod. Phys. **82**, 3045 (2010).

[10] X.-L. Qi and S.-C. Zhang, Topological insulators and superconductors, Rev. Mod. Phys. **83**, 1057 (2011).

[11] X. Zhang, Z.-K. Lin, H.-X. Wang, Z. Xiong, Y. Tian, M.-H. Lu, Y.-F. Chen, and J.-H. Jiang, Symmetry-protected hierarchy of anomalous multipole topological band gaps in nonsymmorphic metacrystals, Nat. Commun. **11**, 65 (2020).

[12] S. H. Kooi, G. van Miert, and C. Ortix, Hybrid-order topology of weak topological insulators, Phys. Rev. B **102**, 041122(R) (2020).

[13] P. Szumniak, D. Loss, and J. Klinovaja, Hinge modes and surface states in second-order topological three-dimensional quantum Hall systems induced by charge density modulation, Phys. Rev. B **102**, 125126 (2020).

[14] Y. Yang, J. Lu, M. Yan, X. Huang, W. Deng, and Z. Liu, Hybrid-Order Topological Insulators in a Phononic Crystal, Phys. Rev. Lett. **126**, 156801 (2021).

[15] S. Murakami, Phase transition between the quantum spin Hall and insulator phases in 3D: Emergence of a topological gapless phase, New J. Phys. **9**, 356 (2007).

[16] X. Wan, A. M. Turner, A. Vishwanath, and S. Y. Savrasov, Topological semimetal and Fermi-arc surface states in the electronic structure of pyrochlore iridates, Phys. Rev. B **83**, 205101 (2011).

[17] K.-Y. Yang, Y.-M. Lu, and Y. Ran, Quantum Hall effects in a Weyl semimetal: Possible application in pyrochlore iridates, Phys. Rev. B **84**, 075129 (2011).

[18] A. A. Burkov and L. Balents, Weyl Semimetal in a Topological Insulator Multilayer, Phys. Rev. Lett. **107**, 127205 (2011).

[19] S. Murakami, M. Hirayama, R. Okugawa, and T. Miyake, Emergence of topological semimetals in gap closing in semiconductors without inversion symmetry, Sci. Adv. **3**, e1602680 (2017).

[20] Z. Wang, Y. Sun, X.-Q. Chen, C. Franchini, G. Xu, H. Weng, X. Dai, and Z. Fang, Dirac semimetal and topological phase transitions in A_3Bi (A = Na, K, Rb), Phys. Rev. B **85**, 195320 (2012).

[21] S. M. Young, S. Zaheer, J. C. Y. Teo, C. L. Kane, E. J. Mele, and A. M. Rappe, Dirac Semimetal in Three Dimensions, Phys. Rev. Lett. **108**, 140405 (2012).

[22] J. A. Steinberg, S. M. Young, S. Zaheer, C. L. Kane, E. J. Mele, and A. M. Rappe, Bulk Dirac Points in Distorted Spinels, Phys. Rev. Lett. **112**, 036403 (2014).

[23] P. Hosur, Friedel oscillations due to Fermi arcs in Weyl semimetals, Phys. Rev. B **86**, 195102 (2012).

[24] G. Xu, H. Weng, Z. Wang, X. Dai, and Z. Fang, Chern Semimetal and the Quantized Anomalous Hall Effect in $\mathrm{HgCr_2Se_4}$, Phys. Rev. Lett. **107**, 186806 (2011).

[25] T. Ojanen, Helical Fermi arcs and surface states in time-reversal invariant Weyl semimetals, Phys. Rev. B **87**, 245112 (2013).

[26] R. Okugawa and S. Murakami, Dispersion of Fermi arcs in Weyl semimetals and their evolutions to Dirac cones, Phys. Rev. B **89**, 235315 (2014).

[27] M. Ezawa, Higher-Order Topological Insulators and Semimetals on the Breathing Kagome and Pyrochlore Lattices, Phys. Rev. Lett. **120**, 026801 (2018).

[28] M. Lin and T. L. Hughes, Topological quadrupolar semimetals, Phys. Rev. B **98**, 241103(R) (2018).

[29] D. Călugăru, V. Juričić, and B. Roy, Higher-order topological phases: A general principle of construction, Phys. Rev. B **99**, 041301(R) (2019).

[30] B. J. Wieder, Z. Wang, J. Cano, X. Dai, L. M. Schoop, B. Bradlyn, and B. A. Bernevig, Strong and fragile topological Dirac semimetals with higher-order Fermi arcs, Nat. Commun. **11**, 627 (2020).

[31] C.-Z. Li, A.-Q. Wang, C. Li, W.-Z. Zheng, A. Brinkman, D.-P. Yu, and Z.-M. Liao, Reducing Electronic Transport Dimension to Topological Hinge States by Increasing Geometry Size of Dirac Semimetal Josephson Junctions, Phys. Rev. Lett. **124**, 156601 (2020).

[32] Q.-B. Zeng, Y.-B. Yang, and Y. Xu, Higher-order topological insulators and semimetals in generalized Aubry-André-Harper models, Phys. Rev. B **101**, 241104(R) (2020).

[33] A. L. Szabó and B. Roy, Dirty higher-order Dirac semimetal: Quantum criticality and bulk-boundary correspondence, Phys. Rev. Research **2**, 043197 (2020).

[34] B. Roy, Antiunitary symmetry protected higher-order topological phases, Phys. Rev. Research **1**, 032048(R) (2019).

[35] S. A. A. Ghorashi, T. Li, and T. L. Hughes, Higher-Order Weyl Semimetals, Phys. Rev. Lett. **125**, 266804 (2020).

[36] H.-X. Wang, Z.-K. Lin, B. Jiang, G.-Y. Guo, and J.-H. Jiang, Higher-Order Weyl Semimetals, Phys. Rev. Lett. **125**, 146401 (2020).

[37] R. Fleury, The sound of Weyl hinges, Nat. Mater. **20**, 716 (2021).

[38] L. Luo, H.-X. Wang, Z.-K. Lin, B. Jiang, Y. Wu, F. Li, and J.-H. Jiang, Observation of a phononic higher-order Weyl semimetal, Nat. Mater. **20**, 794 (2021).

[39] Q. Wei, X. Zhang, W. Deng, J. Lu, X. Huang, M. Yan, G. Chen, Z. Liu, and S. Jia, Higher-order topological semimetal in acoustic crystals, Nat. Mater. **20**, 812 (2021).

[40] Z.-Q. Zhang, B.-L. Wu, C.-Z. Chen, and H. Jiang, Global phase diagram of disordered higher-order Weyl semimetals, Phys. Rev. B **104**, 014203 (2021).

[41] W. B. Rui, S.-B. Zhang, M. M. Hirschmann, Z. Zheng, A. P. Schnyder, B. Trauzettel, and Z. D. Wang, Higher-order Weyl superconductors with anisotropic Weyl-point connectivity, Phys. Rev. B **103**, 184510 (2021).

[42] M. Geier, L. Trifunovic, M. Hoskam, and P. W. Brouwer, Second-order topological insulators and superconductors with an order-two crystalline symmetry, Phys. Rev. B **97**, 205135 (2018).

[43] F. K. Kunst, G. van Miert, and E. J. Bergholtz, Lattice models with exactly solvable topological hinge and corner states, Phys. Rev. B **97**, 241405(R) (2018).

[44] F. Schindler, Z. Wang, M. G. Vergniory, A. M. Cook, A. Murani, S. Sengupta, A. Y. Kasumov, R. Deblock, S. Jeon, I. Drozdov, H. Bouchiat, S. Guéron, A. Yazdani, B. A. Bernevig, and T. Neupert, Higher-order topology in bismuth, Nat. Phys. **14**, 918 (2018).

[45] B.-Y. Xie, H.-F. Wang, H.-X. Wang, X.-Y. Zhu, J.-H. Jiang, M.-H. Lu, and Y.-F. Chen, Second-order photonic topological insulator with corner states, Phys. Rev. B **98**, 205147 (2018).

[46] M. Serra-Garcia, V. Peri, R. Süsstrunk, O. R. Bilal, T. Larsen, L. G. Villanueva, and S. D. Huber, Observation of a phononic quadrupole topological insulator, Nature (London) **555**, 342 (2018).

[47] C. W. Peterson, W. A. Benalcazar, T. L. Hughes, and G. Bahl, A quantized microwave quadrupole insulator with topologically protected corner states, Nature (London) **555**, 346 (2018).

[48] S. Imhof, C. Berger, F. Bayer, J. Brehm, L. W. Molenkamp, T. Kiessling, F. Schindler, C. H. Lee, M. Greiter, T. Neupert, and R. Thomale, Topolectrical-circuit realization of topological corner modes, Nat. Phys. **14**, 925 (2018).

[49] Y. Peng and G. Refael, Floquet Second-Order Topological Insulators from Nonsymmorphic Space-Time Symmetries, Phys. Rev. Lett. **123**, 016806 (2019).

[50] Z. Wang, B. J. Wieder, J. Li, B. Yan, and B. A. Bernevig, Higher-Order Topology, Monopole Nodal Lines, and the Origin of Large Fermi Arcs in Transition Metal Dichalcogenides $X\mathrm{Te}_2$ ($X = \mathrm{Mo, W}$), Phys. Rev. Lett. **123**, 186401 (2019).

[51] X.-L. Sheng, C. Chen, H. Liu, Z. Chen, Z.-M. Yu, Y. X. Zhao, and S. A. Yang, Two-Dimensional Second-Order Topological Insulator in Graphdiyne, Phys. Rev. Lett. **123**, 256402 (2019).

[52] A. Agarwala, V. Juričić, and B. Roy, Higher-order topological insulators in amorphous solids, Phys. Rev. Research **2**, 012067(R) (2020).

[53] R. Chen, C.-Z. Chen, J.-H. Gao, B. Zhou, and D.-H. Xu, Higher-Order Topological Insulators in Quasicrystals, Phys. Rev. Lett. **124**, 036803 (2020).

[54] T. Fukui and Y. Hatsugai, Entanglement polarization for the topological quadrupole phase, Phys. Rev. B **98**, 035147 (2018).

[55] R. Okugawa, S. Hayashi, and T. Nakanishi, Second-order topological phases protected by chiral symmetry, Phys. Rev. B **100**, 235302 (2019).

[56] A. K. Ghosh, G. C. Paul, and A. Saha, Higher order topological insulator via periodic driving, Phys. Rev. B **101**, 235403 (2020).

[57] M. Hirayama, R. Takahashi, S. Matsuishi, H. Hosono, and S. Murakami, Higher-order topological crystalline insulating phase and quantized hinge charge in topological electride apatite, Phys. Rev. Research **2**, 043131 (2020).

[58] C. Chen, Z. Song, J.-Z. Zhao, Z. Chen, Z.-M. Yu, X.-L. Sheng, and S. A. Yang, Universal Approach to Magnetic Second-Order Topological Insulator, Phys. Rev. Lett. **125**, 056402 (2020).

[59] K. v. Klitzing, G. Dorda, and M. Pepper, New Method for High-Accuracy Determination of the Fine-Structure Constant Based on Quantized Hall Resistance, Phys. Rev. Lett. **45**, 494 (1980).

[60] J. Kruthoff, J. de Boer, J. van Wezel, C. L. Kane, and R.-J. Slager, Topological Classification of Crystalline Insulators

through Band Structure Combinatorics, Phys. Rev. X **7**, 041069 (2017).

[61] H. C. Po, A. Vishwanath, and H. Watanabe, Symmetry-based indicators of band topology in the 230 space groups, Nat. Commun. **8**, 50 (2017).

[62] B. Bradlyn, L. Elcoro, J. Cano, M. Vergniory, Z. Wang, C. Felser, M. I. Aroyo, and B. A. Bernevig, Topological quantum chemistry, Nature (London) **547**, 298 (2017).

[63] H. Watanabe, H. C. Po, and A. Vishwanath, Structure and topology of band structures in the 1651 magnetic space groups, Sci. Adv. **4**, eaat8685 (2018).

[64] Z. Song, T. Zhang, Z. Fang, and C. Fang, Quantitative mappings between symmetry and topology in solids, Nat. Commun. **9**, 3530 (2018).

[65] S. Ono and H. Watanabe, Unified understanding of symmetry indicators for all internal symmetry classes, Phys. Rev. B **98**, 115150 (2018).

[66] E. Khalaf, Higher-order topological insulators and superconductors protected by inversion symmetry, Phys. Rev. B **97**, 205136 (2018).

[67] A. Matsugatani and H. Watanabe, Connecting higher-order topological insulators to lower-dimensional topological insulators, Phys. Rev. B **98**, 205129 (2018).

[68] Y. Xu, Z. Song, Z. Wang, H. Weng, and X. Dai, Higher-Order Topology of the Axion Insulator $\mathrm{EuIn_2As_2}$, Phys. Rev. Lett. **122**, 256402 (2019).

[69] Y. Tanaka, R. Takahashi, T. Zhang, and S. Murakami, Theory of inversion-$\mathbb{Z}_4$ protected topological chiral hinge states and its applications to layered antiferromagnets, Phys. Rev. Research **2**, 043274 (2020).

[70] E. Khalaf, H. C. Po, A. Vishwanath, and H. Watanabe, Symmetry Indicators and Anomalous Surface States of Topological Crystalline Insulators, Phys. Rev. X **8**, 031070 (2018).

[71] Y. Tanaka, R. Takahashi, and S. Murakami, Appearance of hinge states in second-order topological insulators via the cutting procedure, Phys. Rev. B **101**, 115120 (2020).

[72] R. Takahashi, Y. Tanaka, and S. Murakami, Bulk-edge and bulk-hinge correspondence in inversion-symmetric insulators, Phys. Rev. Research **2**, 013300 (2020).

[73] M. Ezawa, Magnetic second-order topological insulators and semimetals, Phys. Rev. B **97**, 155305 (2018).

[74] G. van Miert and C. Ortix, Higher-order topological insulators protected by inversion and rotoinversion symmetries, Phys. Rev. B **98**, 081110(R) (2018).

[75] Y. Du, B. Wan, D. Wang, L. Sheng, C.-G. Duan, and X. Wan, Dirac and Weyl Semimetal in XYBi ($X =$ Ba, Eu; $Y =$ Cu, Ag and Au), Sci. Rep. **5**, 14423 (2015).

[76] PYTHON tight-binding open-source package, http://physics.rutgers.edu/pythtb/.

[77] L. Elcoro, B. J. Wieder, Z. Song, Y. Xu, B. Bradlyn, and B. A. Bernevig, Magnetic topological quantum chemistry, Nat. Commun. **12**, 5965 (2021).

[78] B. Peng, Y. Jiang, Z. Fang, H. Weng, and C. Fang, Topological classification and diagnosis in magnetically ordered electronic materials, arXiv:2102.12645.

[79] Z. Wang, H. Weng, Q. Wu, X. Dai, and Z. Fang, Three-dimensional Dirac semimetal and quantum transport in $\mathrm{Cd_3As_2}$, Phys. Rev. B **88**, 125427 (2013).

[80] H. Yi, Z. Wang, C. Chen, Y. Shi, Y. Feng, A. Liang, Z. Xie, S. He, J. He, Y. Peng *et al.*, Evidence of topological surface state in three-dimensional Dirac semimetal $\mathrm{Cd_3As_2}$, Sci. Rep. **4**, 6106 (2014).

[81] M. N. Ali, Q. Gibson, S. Jeon, B. B. Zhou, A. Yazdani, and R. J. Cava, The crystal and electronic structures of $\mathrm{Cd_3As_2}$, the three-dimensional electronic analogue of graphene, Inorg. Chem. **53**, 4062 (2014).

[82] Z. Liu, J. Jiang, B. Zhou, Z. Wang, Y. Zhang, H. Weng, D. Prabhakaran, S. K. Mo, H. Peng, P. Dudin *et al.*, A stable three-dimensional topological Dirac semimetal $\mathrm{Cd_3As_2}$, Nat. Mater. **13**, 677 (2014).

[83] H. C. Po, H. Watanabe, and A. Vishwanath, Fragile Topology and Wannier Obstructions, Phys. Rev. Lett. **121**, 126402 (2018).

[84] A. Altland and M. R. Zirnbauer, Nonstandard symmetry classes in mesoscopic normal-superconducting hybrid structures, Phys. Rev. B **55**, 1142 (1997).

[85] C. Fang, M. J. Gilbert, and B. A. Bernevig, Bulk topological invariants in noninteracting point group symmetric insulators, Phys. Rev. B **86**, 115112 (2012).